Flow Confinement of a Laser Induced Atmospheric Helium Plasma

THESIS

submitted in partial fulfillment of the
requirements for the degree of

BACHELOR OF SCIENCE
in
PHYSICS

Author :	Léon van Velzen
Student ID :	s2037033
Supervisor :	Felix Smits
	Dirk Bouwmeester
2^{nd} corrector :	Michiel de Dood

Leiden, The Netherlands, July 1, 2020

Flow Confinement of a Laser Induced Atmospheric Helium Plasma

Léon van Velzen

Huygens-Kamerlingh Onnes Laboratory, Leiden University
P.O. Box 9500, 2300 RA Leiden, The Netherlands

July 1, 2020

Abstract

Experimentally it has been found that a high power laser pulse focussed on a Helium gas at atmospheric pressure creates a plasma that over time assumes a torus shape. This process could see applications in plasma chemistry and is a first step towards a self-confined magnetohydrodynamics plasma. However, the torus shape is eventually destroyed as cold gas flow from the center of the torus splits the plasma. To study this process the gas dynamics shortly after the laser pulse are reduced to one dimension by applying cylindrical symmetry. The resulting equations are solved numerically. By fitting the one dimensional simulation results to experimental data, a three dimensional starting condition is proposed. Using this starting condition, a three dimensional axi-symmetric simulation is performed which is capable of reproducing both torus formation and splitting. These simulations show that the primary process responsible for torus formation is a low pressure area that is dragged behind the strong shock fronts moving perpendicular to the laser axis. Arguments for the local thermodynamic equilibrium of the plasma are presented. This justifies the application of the Saha equation to find the electron density from the simulated pressures and temperatures. Finally, passive modifications of the plasma environment are considered to prevent the plasma from splitting and provide flow confinement of the plasma for up to 100 µs.

Contents

Symbols and units used

χ	Degree of ionization	
γ	Ratio of specific heats, equal to $\frac{5}{3}$ for Helium	
λ	Mean free path	m
μ	Dynamic viscosity	Pa s
ρ	Density	$\mathrm{kg/m^3}$
$\mathbf{v}$	Velocity vector	$\mathrm{m\,s^{-1}}$
E_i	Helium first ionization energy	J
k_B	Boltzmann constant	$\mathrm{J\,K^{-1}}$
p	Pressure	Pa
r_{He}	Kinetic radius of Helium	m
c	Speed of sound in Helium	$\mathrm{m\,s^{-1}}$
e	Energy per unit mass	$\mathrm{J\,kg^{-1}}$
n	Number density of helium atoms	$\mathrm{m^{-3}}$
T	Temperature	K
V	Volume	$\mathrm{m^3}$

Acknowledgements

I would like to thank Felix Smits for being a dedicated supervisor and for the many productive discussions that have helped to guide my research. Also many thanks to Vincent Kooij for producing and making available the experimental (meta)data that I have used throughout this thesis. I would like to thank Leiden University and especially Dirk Bouwmeester for creating a research environment which enabled me to make a meaningful contribution and take my first step as a scientist.

Chapter 1

Introduction

Laboratory plasmas have been used successfully to convert greenhouse gasses into usable products [1]. However, the energy efficiency of the process leaves considerable room for improvement. One possible reason for the loss of energy is the dispersion of the plasma along the length of the cylindrical container used. A remedy for this problem is to contain the plasma to a toroidal shape. In this thesis the creation and properties of a toroidally shaped plasma is studied by matching computer simulations to available experimental data and thereby reproducing the torus formation numerically. Besides chemical applications the study of a toroidal plasma has the potential to contribute to research on nuclear fusion. In fact, magnetohydrodynamics simulations [2] reveal plasma configurations with nested toroidal flux surfaces and linked magnetic fields which have desirable stability properties.

Experimentally it has been found that the creation of a plasma torus with a short lifespan (less than 100 µs) can be achieved by focusing a laser pulse. Unfortunately the plasma assumes the shape of a torus during only a short timespan ($\sim$ 10 µs). As data analysis of CCD images taken of the plasma show, the torus splits by cold gas moving radially outward from the torus center. In this thesis CCD images taken of the plasma emission following a laser pulse of 250 $\sim$ 275mJ focussed at a Helium gas at atmospheric pressure are used to reconstruct a three dimensional gas flow simulation capable of reproducing both torus formation and splitting. Arguments for the local thermodynamic equilibrium of the plasma are presented and used to justify the use of the Saha ionization equation from the pressure and temperature profiles obtained by simulation. This procedure results

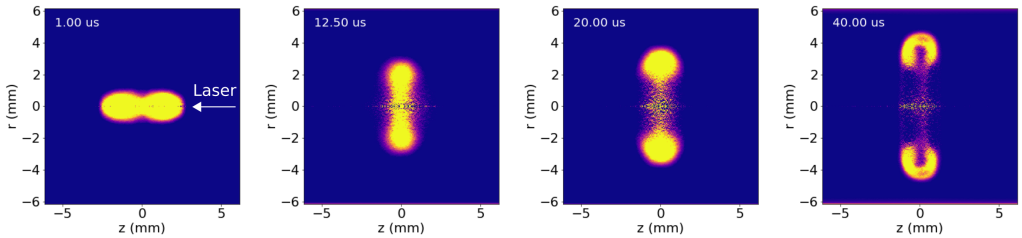

Figure 1.1: *CCD images of the plasma emission are processed to obtain 'slices' of the three dimensional plasma. The way these images are produced is explained in detail in later sections. By cylindrical symmetry the circles in the third image represent a torus shape in three dimensions. The left top corner shows the approximate time that has passed since the laser pulse. Notice the splitting of the plasma in the last image.*

in the electron density profile of the plasma toroid which enables calculation of the plasma resistivity for research on microwave heating of the plasma.

To prevent the plasma from splitting and improve its lifetime from the current $\sim 60\,\mu s$, the plasma environment is modified with passive components to affect the gas flow.

Chapter 2

Previous Experiments

2.1 Experimental Setup

The experimental setup, outlined in figure 2.1 consists of a high power pulsed laser directed towards a vacuum chamber which is filled with helium at atmospheric pressure. The power of the laser used is $250 \sim 275$mJ. The laser is focussed using a 50 mm lens which produces an electromagnetic intensity at the focus that is high enough to ionize the Helium atoms within the timespan of the pulse. The evolution of the resulting plasma with time can be studied through images taken by the CCD camera. Since individual plasmas are not entirely uniform, the CCD camera averages 50 images at a predetermined amount of time after different laser pulses.

2.2 Available Data

Because this thesis is written in the midst of a global pandemic, unfortunately no new experimental data can be presented. However, two key pieces of previously obtained data are available to set up a numerical study of the plasma evolution.

The first of this data consists of schlieren images, which are presented and analyzed in section 4.1. The schlieren images allow accurate tracking of the shock fronts produced by the laser energy deposition.

Furthermore, radiation intensity images taken by the CCD camera show the plasma evolving with time. The CCD images are a side view of the

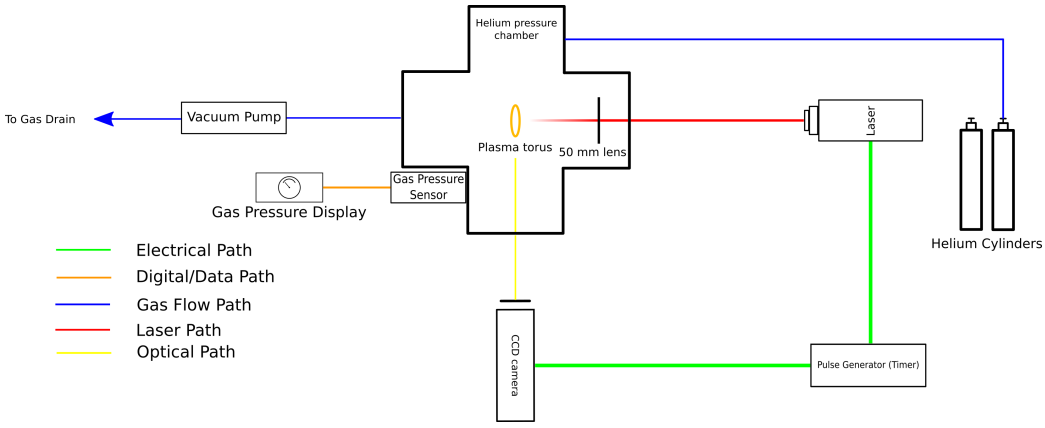

Figure 2.1: *Outline of the experimental setup used to produce the data used as verification material for the simulations. The schlieren images are produced by extending this setup with a knife edge and appropriate background lightning.*

.

plasma. These images together with the cylindrical symmetry of the plasma enables the determination of the local emission intensity. To achieve this an inverse abel transformation is needed, as explained in section 4.3.

Chapter 3

One Dimensional Modelling of the Laser-Induced Explosion

3.1 Bounds on the Pressure Buildup Inside the Plasma

For a crude approximation of average initial gas pressure we assume the plasma to be a cylinder with dimensions determined from an intensity image taken shortly ($\sim 100\,\text{ns}$) after the laser pulse. The dimensions used are presented in figure 3.1. This corresponds to a volume of $V = 6.8\,\text{mm}^3$. Since the laser pulse duration is only 10 ns, the number density of helium atoms in the produced plasma will at first be equivalent to the number density at ambient pressure $n \approx 2.5 \times 10^{25}\,\text{m}^{-3}$. Assuming the full 275 mJ of energy produced by the short laser pulse is converted into heat, while the degree of ionization remains low, the ideal gas law predicts a pressure of $\sim 2.7 \times 10^2$ atm while the temperature rises to $\sim 8.0 \times 10^5$ K. At the other extreme, assume the laser is very effective at ionizing the nV particles present in the emerging plasma. Since producing one singly ionized helium atom requires an energy of 24.6 eV the complete ionization of the volume implies a deposition of $\sim 6.5 \times 10^2$ mJ, which is more than the energy available in the laser pulse. Therefore we can conclude that we can not put stricter bounds on the average initial plasma pressure than between ambient pressure and $\sim 2.7 \times 10^2$ atm.

The commercial Comsol Multiphysics simulation software is used to investigate the mechanisms of torus formation and the energy needed to

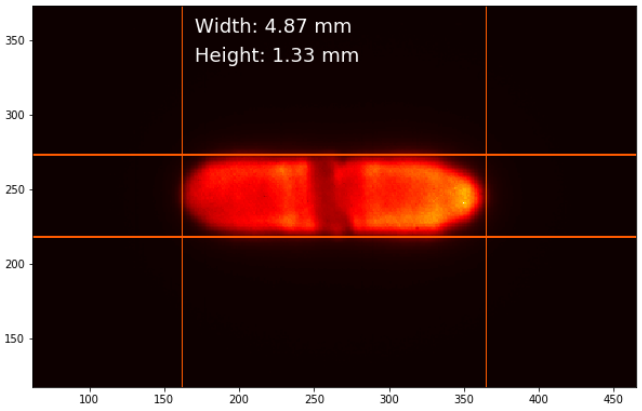

Figure 3.1: *CCD image of the laser induced plasma approximately 100* ns *after the laser pulse. The colormap used is linear and the units arbitrary. The laser comes in from the right. The pixel dimensions are 24.2* mm/pixel *in the vertical direction and 24.0* mm/pixel *in the horizontal direction. This allowed the determination of the dimensions shown in the image. Vertical and horizontal lines were drawn in software.*

match the experimentally determined torus dimension. The Comsol software supports a two dimensional axi-symmetrical simulation mode, saving much time with respect to a full three dimensional simulation. Unfortunately, it is found that the Comsol software runs into divergence issues at pressures much below the maximum 2.7×10^2 atm.

To get better insight into the gas flow shortly after the laser pulse and to obtain insight into the numerical challenges involved the problem is reduced to one dimension and solved numerically. Later we'll use the results of the one dimensional model to help Comsol get past initial divergence problems.

To reduce the problem to one dimension, notice from figure 3.1 that the laser-induced explosion has a high degree of cylindrical symmetry close

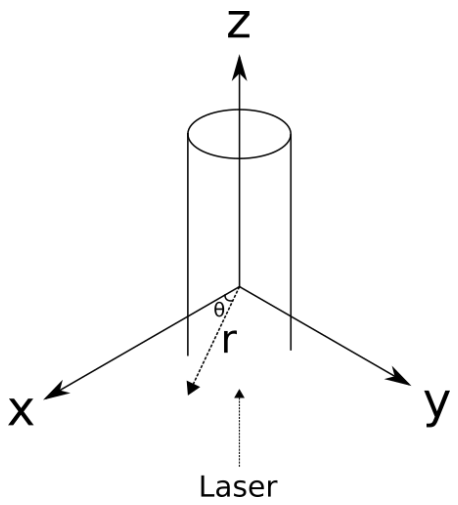

Figure 3.2: *To reduce the problem to one dimension, an infinite cylindrical explosion is computed numerically. The laser pulse is coaxial with the cylindrical explosion and the z-axis. The axis along which the gas state is computed in the simulation is the x-axis, corresponding to $\theta = 0$, $z = 0$. In spherical coordinates the explosion is a point explosion, where we choose ϕ as our angle with the z-axis.*

to the laser focus. Furthermore at the 'edges' of the cylinder the explosion takes on a spherical shape. By using this symmetry we can deduce the gas flow dynamics just after the laser pulse. To do this we bear in mind that a large energy deposition will lead to a radial gas expansion and assume all gas flow is parallel to $\hat{\mathbf{r}}$ in cylindrical or spherical coordinates. Now the flow needs to be computed only along one line which extends radially outward. The cartesian $\hat{\mathbf{x}}$ coordinate axis fulfills these requirements, see figure 3.2.

In this manner the central region of the energy deposition is approximated using an infinite line explosion, while the spherical edges are independently computed as point explosions. To perform the numerical simulation we need the Navier-Stokes equations in one dimension expressed in both cylindrical and spherical coordinate systems.

3.2 Navier-Stokes Equations

In one dimension and neglecting heat conduction and radiation losses the Navier-Stokes equations are given in cartesian coordinates by [3]

$$\frac{\partial \rho}{\partial t} = -\boldsymbol{\nabla} \cdot (\rho \mathbf{v}) \tag{3.1}$$

$$\frac{\partial (\rho u)}{\partial t} = -\boldsymbol{\nabla} \cdot (\rho u \mathbf{v}) - \frac{\partial p}{\partial x} + \frac{\partial}{\partial x}\left(2\mu \frac{\partial u}{\partial x}\right) \tag{3.2}$$

$$\frac{\partial (\rho e)}{\partial t} = -\boldsymbol{\nabla} \cdot (\rho e \mathbf{v}) - p(\boldsymbol{\nabla} \cdot \mathbf{v}) + 2\mu \left(\frac{\partial u}{\partial x}\right)^2 \tag{3.3}$$

Where e is the energy per unit mass and $\mathbf{v} = u\hat{\mathbf{x}}$ is the velocity vector. The divergence terms have not been expanded to simplify the conversion to spherical and cylindrical coordinates. In order to close this system of equations an equation of state is needed. We assume an ideal gas for which we can write

$$pV = Nk_B T$$

While by the equipartition theorem

$$E_{tot} = N \cdot f \cdot \frac{1}{2} k_B T = \frac{1}{\gamma - 1} N k_B T \;\Rightarrow\; \rho e = \frac{E_{tot}}{V} = \frac{p}{(\gamma - 1)}$$

Where $f = 3$ is the number of degrees of freedom of the Helium atoms $\gamma = \frac{5}{3}$ is the ratio of specific heats for Helium, e is the energy per unit mass and E_{tot} is the thermal energy in the volume V. By explicitly using γ our equations are not specific to Helium. Substituting $\rho e = \frac{p}{\gamma - 1}$ into equation 3.3 we find

Gas flow equations in cartesian coordinates

$$\frac{\partial \rho}{\partial t} = -\frac{\partial (\rho u)}{\partial x} \tag{3.4}$$

$$\frac{\partial (\rho u)}{\partial t} = -\frac{\partial (\rho u^2)}{\partial x} - \frac{\partial p}{\partial x} + \frac{\partial}{\partial x}\left(2\mu \frac{\partial u}{\partial x}\right) \tag{3.5}$$

$$\frac{\partial p}{\partial t} = -\frac{\partial (pu)}{\partial x} - (\gamma - 1) p \frac{\partial u}{\partial x} + 2(\gamma - 1)\mu \left(\frac{\partial u}{\partial x}\right)^2 \tag{3.6}$$

To convert the gas flow equations to cylindrical coordinates we observe that for a given quantity α by the chain rule

$$\frac{\partial \alpha}{\partial x} = \frac{\partial \alpha}{\partial r}\frac{\partial r}{\partial x} + \frac{\partial \alpha}{\partial \theta}\frac{\partial \theta}{\partial x} + \frac{\partial \alpha}{\partial z}\frac{\partial z}{\partial x}$$

But by our assumed cylindrical symmetry $\frac{\partial \alpha}{\partial \theta} = \frac{\partial \alpha}{\partial z} = 0$. Furthermore we can choose to do the simulation along the $\theta = z = 0$ axis so that $\frac{\partial r}{\partial x} = \cos\theta = 1$. We thus find that the derivatives of the Navier-Stokes equations can be converted to cylindrical coordinates by the simple substitution

$$\frac{\partial \alpha}{\partial x} \Rightarrow \frac{\partial \alpha}{\partial r}$$

To convert the divergence terms, one can consult a calculus book to find

$$\boldsymbol{\nabla} \cdot \mathbf{A} = \frac{1}{r}\frac{\partial (rA_r)}{\partial r} + \frac{1}{r}\frac{\partial A_\theta}{\partial \theta} + \frac{\partial A_z}{\partial z}$$

Again, by assumed symmetry the last two terms vanish. To conclude, the equations we solve for are

Gas flow equations in cylindrical coordinates

$$\frac{\partial \rho}{\partial t} = -\frac{1}{r}\frac{\partial (r\rho u)}{\partial r} \tag{3.7}$$

$$\frac{\partial (\rho u)}{\partial t} = -\frac{1}{r}\frac{\partial (r\rho u^2)}{\partial r} - \frac{\partial p}{\partial r} + \frac{\partial}{\partial r}\left(2\mu \frac{\partial u}{\partial r}\right) \tag{3.8}$$

$$\frac{\partial p}{\partial t} = -\frac{1}{r}\frac{\partial (rpu)}{\partial r} - (\gamma - 1)\frac{p}{r}\frac{\partial (ru)}{\partial r} + 2(\gamma - 1)\mu \left(\frac{\partial u}{\partial r}\right)^2 \tag{3.9}$$

Where in this case $\mathbf{v} = u\hat{\mathbf{r}}$.

In spherical coordinates the story is much the same. Only this time the divergence is given by

$$\boldsymbol{\nabla} \cdot \mathbf{A} = \frac{1}{r^2}\frac{\partial (r^2 A_r)}{\partial r} + \frac{1}{r\sin\theta}\frac{\partial}{\partial \theta}(A_\theta \sin\theta) + \frac{1}{r\sin\theta}\frac{\partial A_\phi}{\partial \phi}$$

Where the last two terms vanish since the initial condition is spherically symmetric and we choose to simulate the $\theta = \frac{1}{2}\pi$, $\phi = 0$ axis.

Version of July 1, 2020– Created July 1, 2020 - 11:37

Gas flow equations in spherical coordinates

$$\frac{\partial \rho}{\partial t} = -\frac{1}{r^2}\frac{\partial (r^2 \rho u)}{\partial r} \tag{3.10}$$

$$\frac{\partial (\rho u)}{\partial t} = -\frac{1}{r^2}\frac{\partial (r^2 \rho u^2)}{\partial r} - \frac{\partial p}{\partial r} + \frac{\partial}{\partial r}\left(2\mu \frac{\partial u}{\partial r}\right) \tag{3.11}$$

$$\frac{\partial p}{\partial t} = -\frac{1}{r^2}\frac{\partial (r^2 p u)}{\partial r} - (\gamma - 1)\frac{p}{r^2}\frac{\partial (r^2 u)}{\partial r} + 2(\gamma - 1)\mu \left(\frac{\partial u}{\partial r}\right)^2 \tag{3.12}$$

3.3 Method Used for Computing the Gas Flow Variables

As electrons recombine with Helium ions they emit line radiation. The energy source of this radiation is the potential energy of the electrons, and not the heat of the system. Therefore this process will not have a major influence on the heat of the gas. Furthermore since the simulation is on the order of microseconds heat conductivity and thermal radiation energy loss are assumed to be zero. For Helium the bulk viscosity is zero. The dynamic viscosity is independent of pressure [4] but does have a strong temperature dependence. To account for this, experimental values of [4] and [5] are taken and fitted to Sutherland's law. The result is

$$\mu = 1.86 \cdot 10^{-6} \frac{T^{3/2}}{T + 2.27 \cdot 10^2}$$

The error in this fit is less than 10% at all temperatures for which viscosity data was available.

To compute the viscosity the local temperature is needed. The temperature can be computed using the ideal gas law as

$$T = \frac{m}{k_B}\frac{p}{\rho}$$

Here $m \approx 6.64 \cdot 10^{-27}$ kg is the mass of the helium atom and k_B is the Boltzmann constant.

The gas flow equations are solved using a second order finite difference formula for the spatial derivatives and an explicit time stepping scheme

for the temporal evolution. The time stepping scheme used is a third order Adams-Bashforth method as it is found empirically that for this problem computation times for a given precision are slightly less than those for the more common Runge-Kutta methods. The third order Adams-Bashforth method can be summarized as

$$s_{n+1} = s_n + dt\left(\frac{23}{12}F(s_n) - \frac{4}{3}F(s_{n-1}) + \frac{5}{12}F(s_{n-2})\right)$$

Where s_n is the state (density, velocity and pressure) at timestep n and F is the right hand side of the gas flow equations.

3.4 Verification

To verify that the equations used for the numerical study are correct and no programming errors were made, the results of the simulation are verified in three different ways.

To generate data for these verifications we run a cylindrical simulation with the following starting conditions combined with a grid size $N = 30000$, time step $\Delta t = 0.5 \times 10^{-11}\,\mathrm{s}$.

$$p(r) = 7.5e^{-(r/0.5)^2} + 1\ \mathrm{atm} \tag{3.13}$$

$$u(r) = 0\,\mathrm{m\,s^{-1}} \tag{3.14}$$

$$\rho(r) = 0.164\,\mathrm{kg\,m^{-3}} \tag{3.15}$$

The first and simplest verification is to check whether the physically conserved quantities mass, momentum and energy are actually conserved. The gas flow variables computed at every spatial grid point during the simulation are $\rho, \rho u, p$. The first two quantities can be simply multiplied by the volume corresponding to every grid point (which differs between cylindrical and spherical simulations) and summed to get the total mass and momentum. To find the energy added by the laser energy deposition we compute

$$\frac{3}{2}(p - p_{\mathrm{ambient}}) + \frac{1}{2}\rho u^2 = \frac{3}{2}(p - p_{\mathrm{ambient}}) + \frac{\frac{1}{2}(\rho u)^2}{\rho}$$

to calculate the energy corresponding to a grid point. These energies are again multiplied by the corresponding volume and summed to get the

total energy. It is found that the difference in the mass and momentum at the start and end of the simulation is negligible, with a difference so small it is more likely been caused by floating point rounding errors than programming mistakes. The difference in total energy is slightly larger at around 0.004% but still small enough to not raise any suspicion of faulty programming.

The second verification is a comparison of the shock front speed with the speed predicted by the Rankine-Hugoniot relations. A full derivation of these relationships is outside the scope of this thesis, but we'll briefly mention how the formula used can be derived (see [6] for the full derivation). The Rankine-Hugoniot relations are found by imagining a small rectangular volume around the shock front, and moving along with the front. In the limit that the thickness of the volume around the front goes to zero, and in the limit of a strong shock front so we can neglect viscosity, the quantities momentum, energy and mass stored in the volume must go to zero as well. Therefore these conserved quantities must exit the volume at the 'back' of the shock front as quickly as these quantities enter the volume at the front. This allows to write down an equation for every conserved quantity, and together with the equation for the speed of sound $c = \sqrt{\gamma P/\rho}$, and emit line radiation, they lose their potential energy. Since this potential energy was not present in the form of heat, this results in an expression for the shock front speed as a function of the ratio of the front pressure P and ambient pressure P_{ambient}.

Shock front speed

$$v_{\text{front}} = c\sqrt{\frac{\gamma+1}{2\gamma}\left(\frac{p_{\text{front}}}{p_{\text{ambient}}} - 1\right) + 1} \tag{3.16}$$

As the front observed in our simulation is very sharp, the approximation made in the derivation of the Rankine-Hugoniot relations is good. Therefore as a verification of our simulation we can compute the shock front speed from the pressure at the shock front and see if the shock front in our simulation indeed moves at this velocity. This verification is illustrated in figure 3.3, which shows that the correspondence is indeed very good.

As a third and final verification, we compare the one dimensional simulation with a two dimensional axi-symmetrical Comsol simulation with the same starting conditions. The result can be seen in figure 3.4. The Comsol simulation seems to lag the one dimensional study in the formation of a

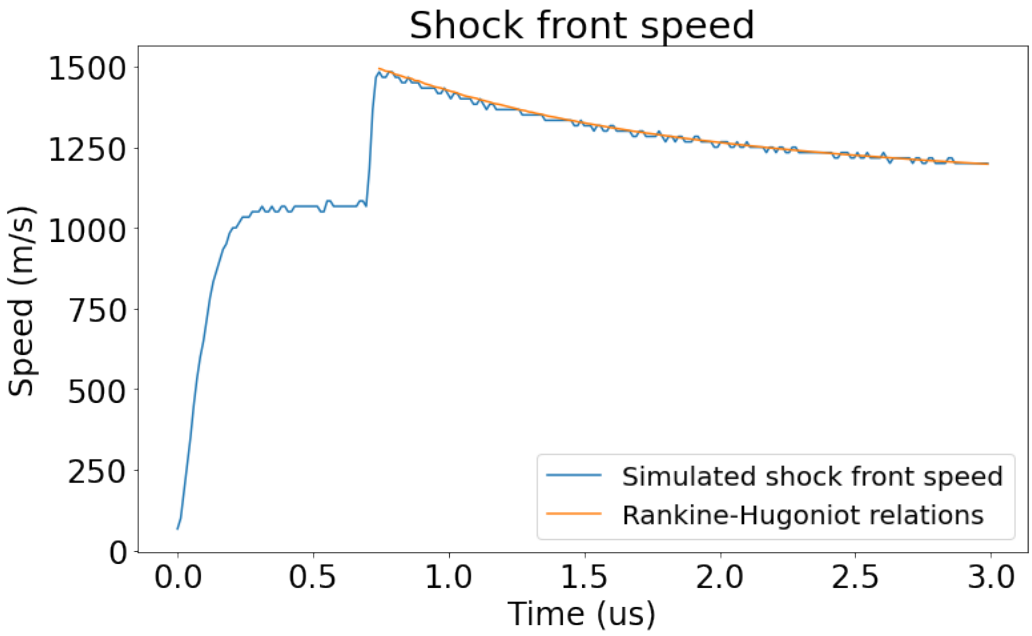

Figure 3.3: *Comparison of theoretically predicted shock front speed with the numerically found speed. The starting conditions of the simulation are given by equations 3.13 to 3.15. As explained later, the gas flow progresses in three distinct phases (pressure collapse, shock front generation and shock front propagation). These phases are clearly visible in this graph. The maximum pressure at every time in the simulation is used to compute the theoretically predicted speed using equation 3.16 and compared with the shock front propagation phase. The correspondence is very good.*

shock front. However, eventually the shock front forms after which both simulations agree to high accuracy. The reason that the Comsol simulation takes a longer time to generate the sharp shock front is not immediately clear. A possible explanation is that the algorithms used by the Comsol software have more numerical diffusion which is known to smooth out shock fronts.

3.5 Results

Experience with the one dimensional simulation have shown the challenge in the numerical study of laser induced gas flow to be twofold. First of all starting the simulation with high initial pressure values seems to immediately cause convergence issues at the start of the simulation. These convergence issues can only be solved by lowering the time step

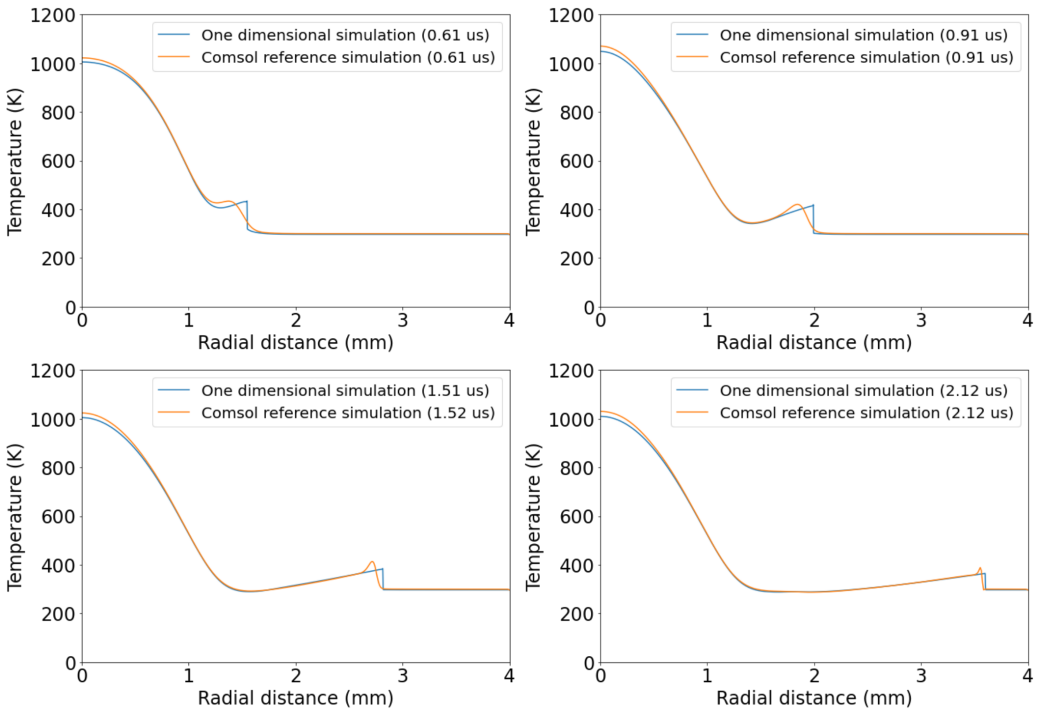

Figure 3.4: *Comparison of the one dimensional numerical study with results predicted by an axi-symmetrical Comsol simulation. The comparison is made by a temperature vs distance plot. The starting conditions are given by equations 3.13 to 3.15. The Comsol simulation seems to be less eager to form a strong shock front early in the simulation. However, eventually the shock front forms after which the correspondence is very good.*

.

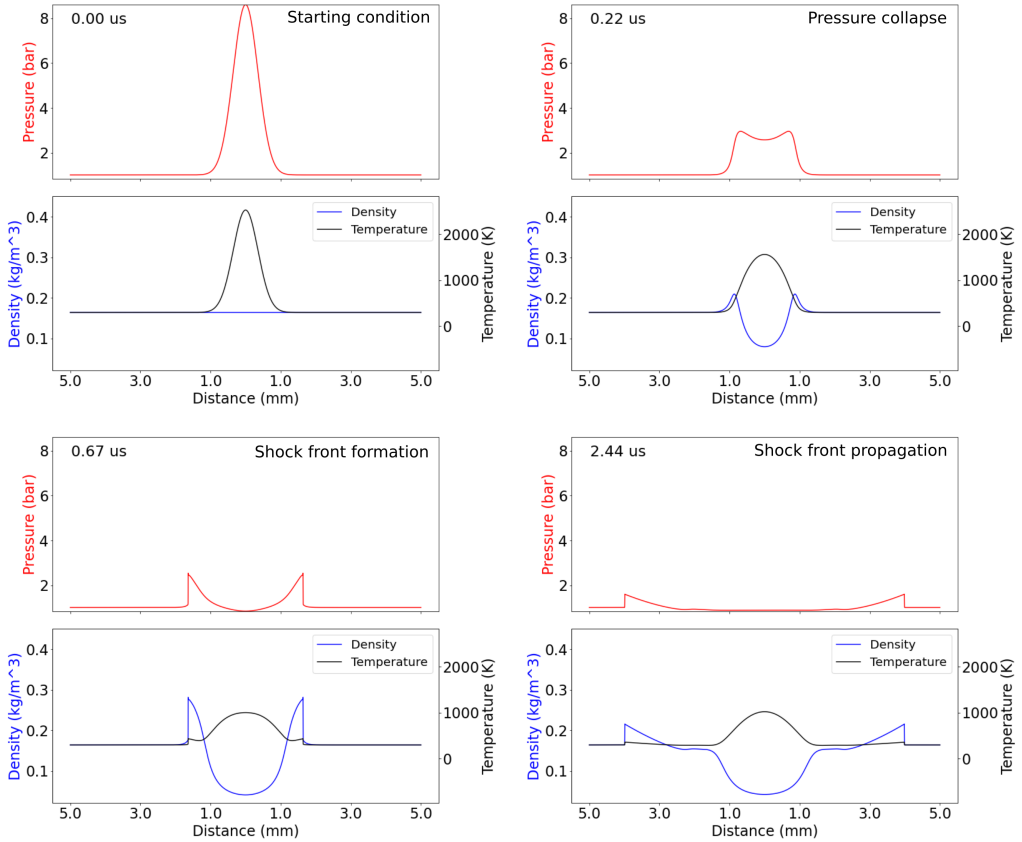

Figure 3.5: *Results of the cylindrically symmetric one dimensional simulation with starting condition given by 3.13 to 3.14. Three different phases can be observed in the development of the gas flow variables. In the pressure collapse phase the pressure peak developed at $r = 0$ is found to be unstable. The peak collapses resulting in an outward motion of the gas. In the shock front formation phase this outward motion becomes so strong that sharp shock fronts arise moving radially outwards. The shock fronts carry away just the right amount of mass to compensate for the high temperature at the center. This causes the centre to regain stability. In the shock front propagation phase therefore only the shock fronts are seen to be moving. Note that the pressure between both shock fronts is slightly below ambient pressure. This drives the backflow of gas towards the plasma later on.*

used throughout the simulation. This problem appears to correspond to the known Courant-Friedrichs-Lewy condition which establishes upper bounds on the time step if divergence is to be avoided.

The second numerical challenge is the very sharp shock fronts that arise as a result of gas expansion. For even moderate pressures the shock front becomes so steep that only a few grid points can be used to resolve the slope of the front. As the front becomes steeper, it becomes more difficult to accurately determine the derivatives of pressure, density and velocity. The result is that the gas flow variables appear to contain discontinuities which in turn causes numerical instability. This instability presents itself in the form of small wave-like errors close to the shock front which remind the author of the Gibbs phenomenon. To overcome this problem the spatial grid size must be chosen very small. However, the Courant-Friedrichs-Lewy condition specifies that a reduction in spatial grid size must be accompanied with a reduction in the time step taken. Therefore there are two different features of the gas flow, namely the high initial pressures and the sharp shock fronts that motivate the time step to be small and thereby increasing computation time.

We now consider the development of the gas flow variables through time as computed in the one dimensional model. For this we consider the cylindrical simulation performed in the verification corresponding to the starting conditions 3.13 to 3.15. The result is shown in figure 3.5. These results suggest that after a central energy deposition the gas flow progresses in what can be considered three different phases.

The first is pressure collapse, in which the high pressure in the middle of the cylinder falls rapidly while gas is pushed in the radial direction. The second phase is shock front production, in which the outer gas layer achieves supersonic speed and forms near vertical shock fronts while continuing to move radially. The third and final phase is shock front propagation. In this phase the departure of the shock fronts seem to have caused stability in the central region and therefore only the shock fronts are seen to be moving. The stability at the center is most clearly exemplified by the near flatness of the pressure graph around $r = 0$.

Stability of the plasma can be understood by considering the ideal gas law $P = \frac{N}{V} k_B T$. Since $\rho \propto \frac{N}{V}$ it is evident that the pressure reaches high values around $t = 0$ since at this point in time the density is equal to the ambient density, while the temperature has increased by a large factor. However, it turns out that the shock front carries away the right amount of matter (decrease in ρ) to bring P back close to ambient pressure.

In a previous experiment of our research group a second laser was used in an attempt to create plasma geometries consisting of multiple tori. It was found however that the second laser was not able to induce a plasma and it was therefore hypothesized that the large energy deposition of the first laser brings the central region to near vacuum or zero pressure. This one dimensional simulation shows that, at least for the small initial energy deposition used in the verification, no vacuum is generated and the pressure quickly falls back to atmospheric pressure. The simulation suggests the actual physical reason preventing a second plasma to be induced is the low density at $r = 0$.

Chapter 4

Simulation of Torus Formation and Subsequent Splitting

In the one dimensional study the main features of the gas flow and the numerical challenges were identified. It was found that the shock fronts moving away from the instantaneously heated gas carried away the right amount of matter to restore stability in the central region. The shock front speed equation 3.16 can also be written in terms of the density at the shock front [6]:

$$v_{\text{front}} = c\sqrt{\frac{2}{(\gamma+1)\frac{\rho_{\text{ambient}}}{\rho_{\text{front}}} + (1-\gamma)}}$$

So we see that the speed of the shock front is related to the amount of matter taken away from the central region and therefore indirectly to the energy deposited by the laser. In other words, the amount of energy deposited determines how much matter is present in the shock front, and the amount of matter in the shock front determines the speed of the front. This knowledge can be exploited by comparing the speed of the shock front as determined by schlieren imaging with the speed found from the one dimensional simulations. This correspondence can be optimized to find the best fit of initial energy for the one dimensional simulation for both the spherical and cylindrical regions of the gas expansion. These two 'best fit' one dimensional simulations can be combined to form a three dimensional initial condition. Convergence issues of Comsol at small time delays after the laser pulse can be circumvented by performing this interpolation at a time $t > 0$ after the pressure collapse phase (see figure 3.5). Unfortunately

it is found that the spherical one dimensional simulation has stability issues itself, with the $\frac{1}{r^2}$ terms present in the equation causing numerical 'blowup' at the pole $r = 0$. To still be able to construct a three dimensional initial condition, results of the cylindrical simulation are used with a suitable weakening at the spherical sections as determined by equation 3.16 and the shock front velocities visible in the schlieren images.

4.1 Comparison with schlieren images

It is clear that we need to extract the shock front positions and speeds as accurately as possible from the schlieren images to enable a comparison with simulation data. As the schlieren images turn out to contain significant amounts of noise a high frequency filter is applied to the image to smooth the noisy pixel intensity values (gaussian filter, sigma $\sim$ 3.25). A straight line is drawn from the center of the plasma at different angles with the laser axis. The values along this line are determined from the image pixels by a second order interpolation. By analysing the graphs resulting from this interpolation a good criterion was sought to identify the peak corresponding to the schlieren shock front. It was found that the shock front in almost all cases coincided with the peak for which the *prominence* divided by the *width* was the highest value. The exact definitions of these terms can be found in the documentation of the *find_peaks* function of SciPy [7]. In the few cases that this method failed to find the correct shock front position for a given frame the position was extrapolated from the position on the prior frame by assuming constant velocity.

The result of this method is illustrated in figure 4.1. It can be seen that the shock front position was determined with good accuracy. After less than one microseconds the shock front is very well approximated by an ellipse. The width and height of the ellipse are plotted as a function of time in figure 4.2. The height of the ellipse corresponds to the shock front position at the cylindrical section of the plasma. As such we can find an initial condition which generates the proper shock fronts by running a one dimensional simulation in cylindrical coordinates and comparing its result with the data obtained from the schlieren images.

Using the position of the shock fronts as a function of time to make the comparison with the one dimensional simulation is vulnerable to large inaccuracies as this method depends on knowing exactly at which moment the schlieren images are taken after the laser pulse. A more reliable method is to determine the speed of the shock front as a function of the

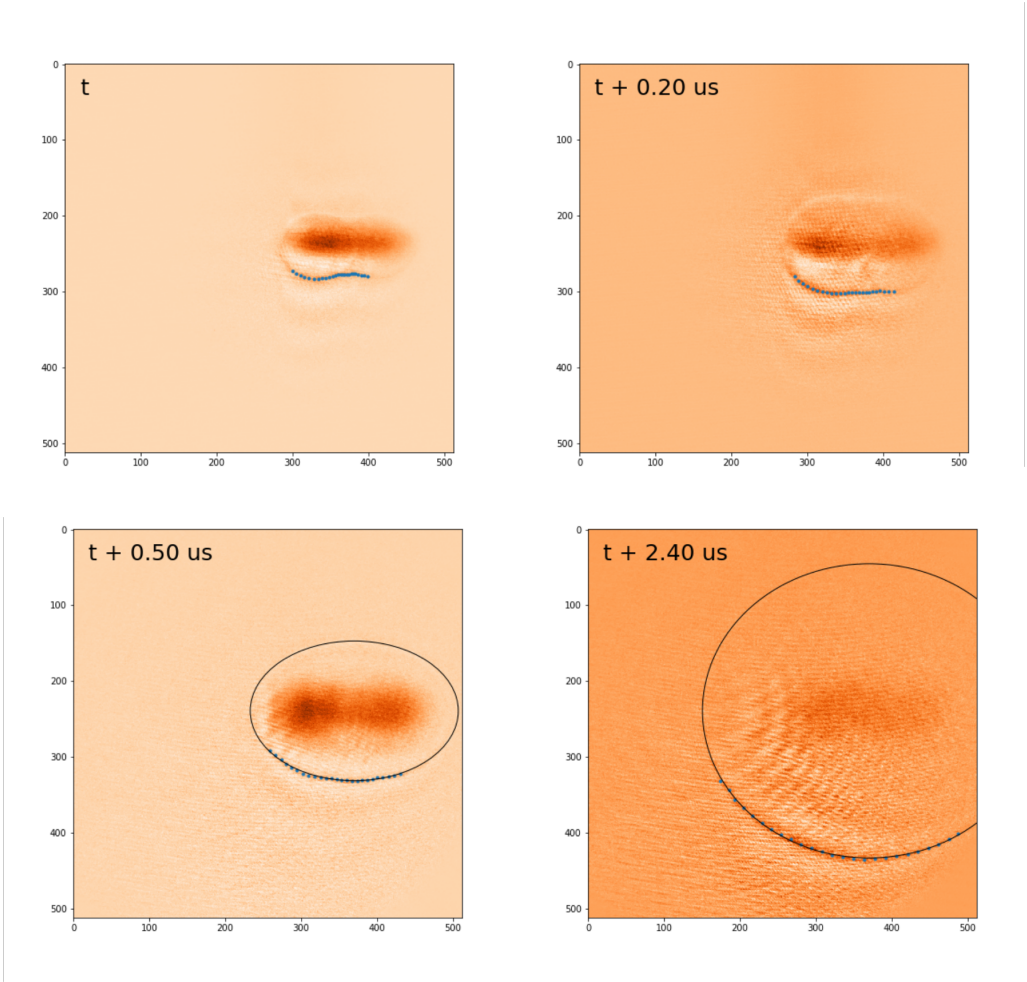

Figure 4.1: *Four frames from a series of schlieren images are selected to show how the distance of the shock front is determined. The full series (files test-t7078.SPE, test-t6975.SPE) contains 87 frames. To uncover the non-static features of the schlieren images a background image without the laser plasma is subtracted from all following frames. Inherent to the schlieren imaging method used, the outward moving shockfront is not visible on the laser axis. The data is used to produce figures 4.2, 4.4 and 4.3.*

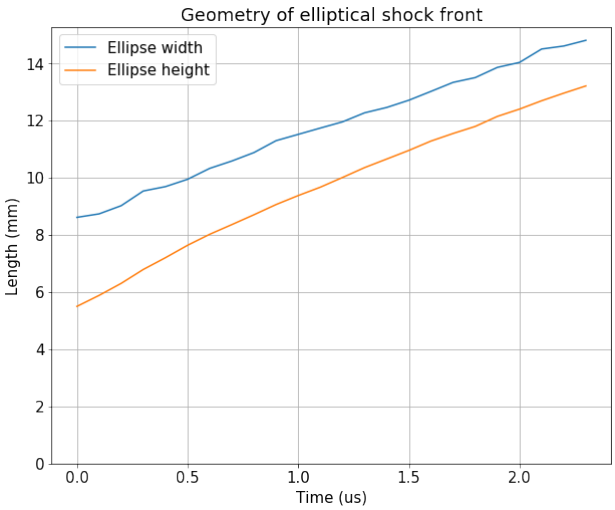

Figure 4.2: *The development of the width and height of the elliptical shock front is shown as a function of time. $t = 0$ is chosen at the first time at which the laser pulse appears a good fit. Notice that the ellipse height increases more rapidly than the width initially, implying a faster and stronger shock front in the direction perpendicular to the laser axis.*

distance from the laser axis. This method only depends on the time between the CCD images to be constant and this is guaranteed by the CCD camera. The position of the laser axis can easily be determined from the schlieren images.

With regards to the gas flow variables ρ, ρu, p of the initial condition of the one dimensional simulation only the pressure p needs to be determined since from the assumption of an instantaneous laser energy deposition the density ρ is equal to the density at atmospheric pressure and room temperature while the gas velocity u is zero. The pressure is assumed to be a sum of atmospheric pressure and a 'peaked' function. To construct these peaked functions with arbitrary widths, sharpness and energy we take A, B and C as free parameters and use the formula

$$p = Ae^{-B|r|^C} \tag{4.1}$$

To make a good comparison between the experimentally determined speed values and the values found numerically we compare the simulation data to a fit to the schlieren data. The simulation's initial pressure is modified until good correspondence is achieved. The question remains which function to use for the fit to the schlieren shock front velocity. Intuitively

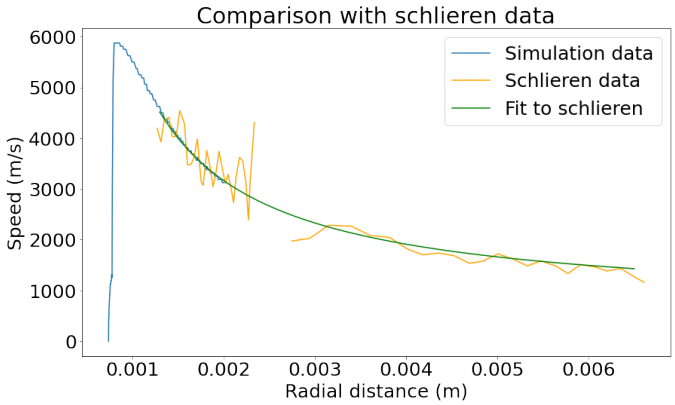

Figure 4.3: *A one dimensional simulation is found that is capable of reproducing the shock front moving outward perpendicular to the laser axis as seen on the schlieren images (see figure 4.1). The starting condition is chosen as equation 4.1. In order not to be vulnerable to inaccuracies in the timing data of the schlieren images the comparison is made using a shock speed vs shock position graph. The starting condition is* $p(t = 0) = 169e^{-15.5|r|^{3.24}}$ *(r in* mm*) and corresponds to the lowest difference in figure 4.4. The function used for the fit (green line) is motivated in the text and has the form* $\frac{a}{r} + b$ *with* $a = 5.016\,\mathrm{m^2\,s^{-1}}$ *and* $b = 657.6\,\mathrm{m\,s^{-1}}$.

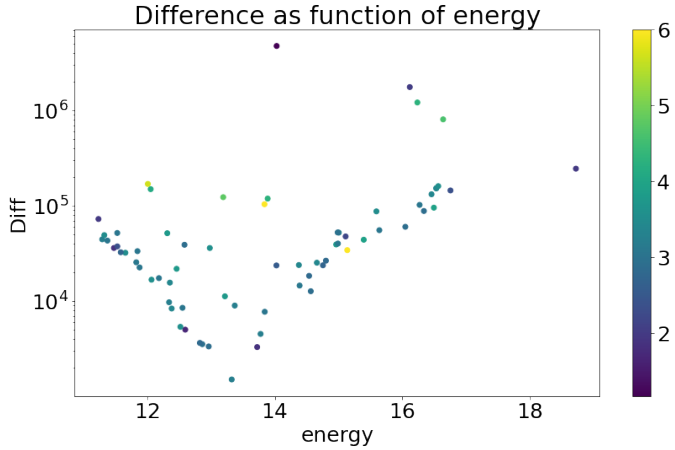

Figure 4.4: *Every point represents a one dimensional simulation. The result of the simulation is compared with the data obtained from the schlieren images to compute a difference. For the procedure used see figure 4.3. The color in the graph is determined by the C parameter in the initial condition, see equation 4.1. The quantitative behaviour of this graph depends on the procedure chosen to compute the difference. However, qualitatively one can see that there is a strong dependence between the energy and the fit with the schlieren data. The energy deposited in the best fit simulation is* $13.3\,\mathrm{J\,m^{-1}}$.

speaking the outgoing momentum of the shock wave is divided over an increasing area as the shock front moves outwards. This would imply a velocity proportional to $\frac{1}{r}$. However, this would imply that the speed would decay to zero as $r \to \infty$ while we know the speed in fact decays to the speed of sound. Therefore, the function chosen for the fit is $\frac{a}{r} + b$ with a and b free parameters. An alternative motivation of this function can be made by considering it as a low order Taylor expansion in the variable $\frac{1}{r}$. In any case, one can see from figure 4.3 that this function follows the simulation data very closely.

Figure 4.4 shows the sum of squares difference between the simulation data and the part of the fit to the schlieren data that overlaps with the simulation. This figure shows clearly the energy dependence discussed earlier. The best fit (lowest y value) simulation in this figure corresponds to the chosen simulation in figure 4.3. In this best simulation the energy deposited by the laser for a cylinder of length L is

$$\frac{E}{L} = \frac{3}{2}pV = \frac{3}{2} \cdot 2\pi \cdot \int_0^\infty 169 \cdot p_{\text{ambient}}\, e^{-15.5\left(\frac{r}{1000}\right)^{3.24}} r\mathrm{d}r = 13.3\,\mathrm{J\,m^{-1}}$$

Where $p_{\text{ambient}} = 101\,325\,\mathrm{Pa}$ is taken as atmospheric pressure. For the cylinder length 4.87 mm in figure 3.1 this corresponds to 64.8 mJ. Figure 4.5 shows the development of the gas flow variables in the simulation corresponding to figure 4.3.

4.2 Reconstruction of the Three Dimensional Initial Condition

A three dimensional initial condition that reproduces the experimentally found shock front can be reconstructed by 'smearing out' the one dimensional simulation over a two dimensional plane. This two dimensional image represents a plane through the laser axis, and therefore its revolution around the laser axis represents the full three dimensional situation. A simulation is subsequently performed using the two dimensional axi-symmetric high mach number laminar flow module of Comsol Multiphysics. If the strength and shape of the shock front is the primary cause of torus formation the simulation should be able to reproduce this. In the rest of this section the method used to reconstruct the two dimensional axi-symmetric initial condition from the one dimensional simulation is explained in depth.

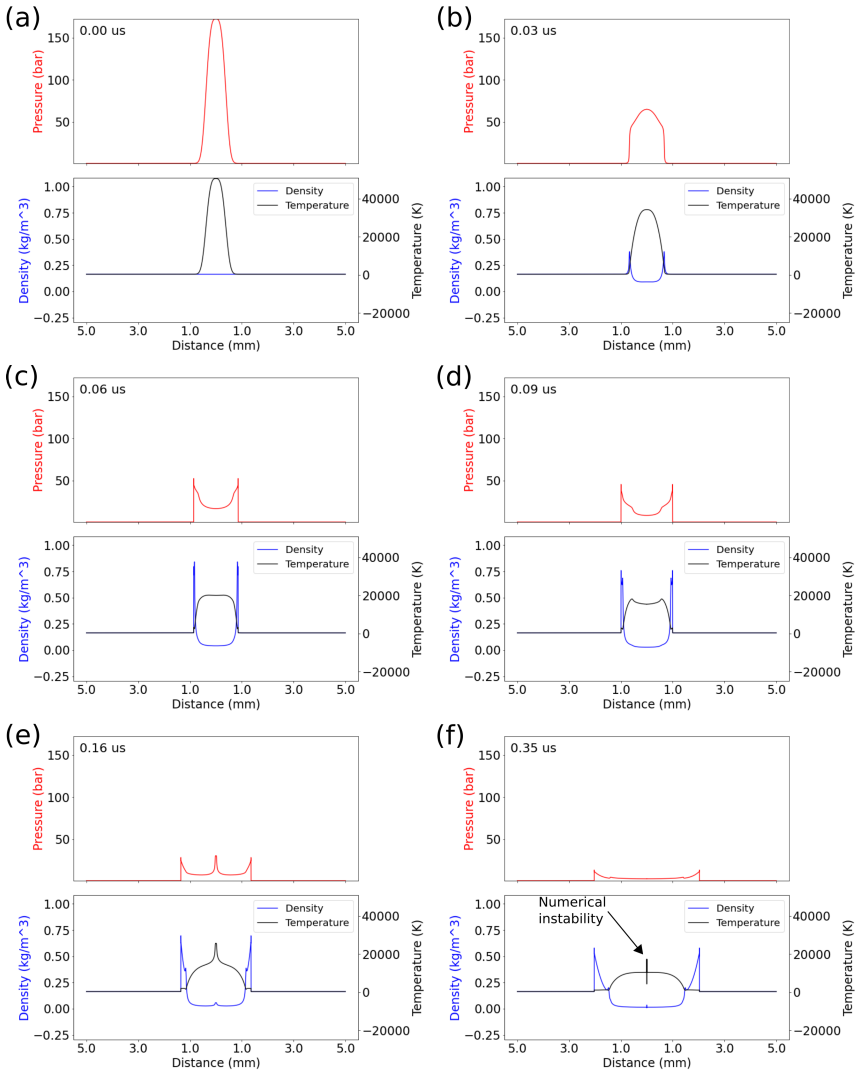

Figure 4.5: *Cylindrical simulation chosen as source from which the three dimensional initial condition is reconstructed ($p(t=0) = 169e^{-15.5|r|^{3.24}}$ with r in* mm*). Notice that the initial expansion results in an inward moving flow that compresses and heats the region near $r = 0$ as seen in image (e). The (second) expansion resulting from this process results in a weak secondary shock front that is also faintly visible in the last image of figure 4.1. Image (f) shows a numerical instability arising near $r = 0$ which eventually forces the simulation to halt. The violent gas dynamics in this simulation cause up to 6.7% of the initial energy to be dissipated numerically, which is 12.7% of the energy added by laser deposition. This last percentage can be considered as the error on the* 58 mJ *initial energy found in the reconstructed initial condition. Further research is necessary to solve the numerical instability and decrease the energy dissipation.*

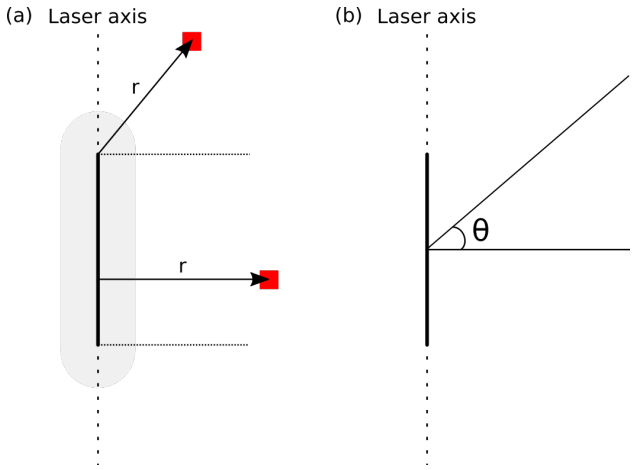

Figure 4.6: *Diagram illustrating the reconstruction of the three dimensional initial condition. (a) The spherical parts of the plasma shown in figure 3.1 are removed to obtain a axial line segment. The length of the line segment is chosen (*3.6 mm*) such that the simulated shock fronts correspond well with those visible on the schlieren images. The distance of every interpolation point to this line segment is used to determine the gas state variables. This distance r is illustrated for two interpolation points shown in red. (b) The angle θ is defined relative to a horizontal line extending from the centre of the line segment.*

The reconstruction is based on three key ingredients; the size of the first good elliptical fit to the schlieren shock front, the cylindrical simulation found in the previous section and the speed of the shock front along the laser axis. The plasma is idealized to have a shape consisting of three sections; two perfect half spheres and a central cylinder. A single state of the one dimensional simulation corresponding to a certain time and peak position r_{peak} is chosen as the *source state*. This *source state* should be chosen 'late' enough to make sure the pressure has collapsed sufficiently to guarantee convergence of the following Comsol simulation. The source state can be considered as a set of functions giving the density, velocity and pressure at the chosen time as a function of the distance to the cylinder axis r. Therefore at every point of the two dimensional axi-symmetric image we need to define a distance that can be used to 'lookup' the corresponding gas variables at that point. This distance is defined in figure 4.6.

However, by the inability of making a proper one dimensional spherical simulation we end up with an axial shock front with strength equal to the shock front perpendicular to the laser axis. This is incorrect as from figure 4.2 it is seen that the ellipse fitted to the shock front increases more rapidly

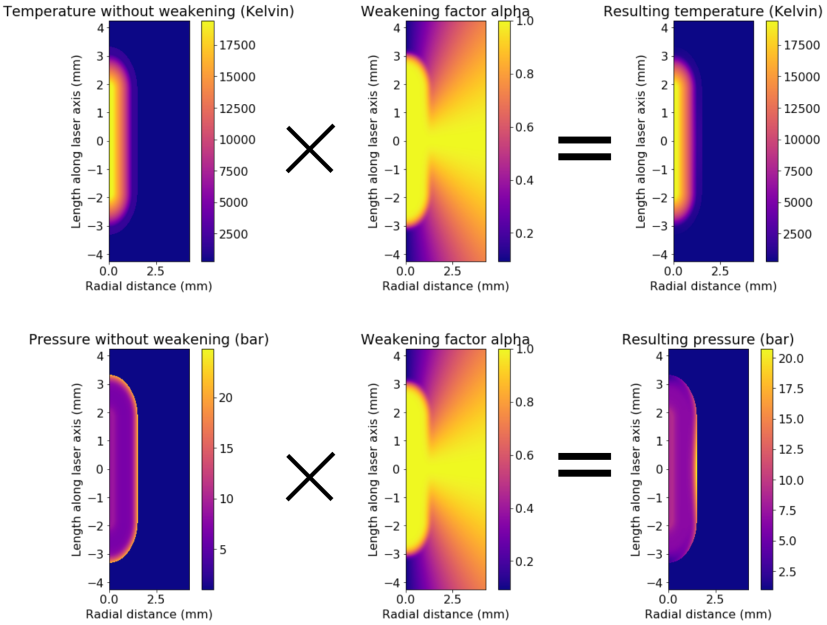

Figure 4.7: *The weakening factor is defined in such a way that the spherical shock fronts are weakened while keeping the core temperature unaffected. The dimension of the plasma is chosen such that the resulting shock front will assume the elliptical shape determined from the schlieren images.*

in *radial direction* than it does in *axial direction*. To make sure the Comsol simulation will end up with the correct shock front positions we choose to weaken the shock front in the axial direction. To do this we define the position dependent weakening factor $0 \leq \alpha(r,\theta) \leq 1$ which we apply at every position of the initial condition in such a manner that the ratio of thermal to kinetic energy stays constant. To know how to do this consider the ideal gas law (u and w are respectively the radial and axial componets of the velocity):

$$\alpha E = \alpha\left(\frac{3}{2}pV + \frac{1}{2}(\rho V)(u^2+w^2)\right) = \frac{3}{2}(\alpha p)V + \frac{1}{2}(\rho V)((\sqrt{\alpha}u)^2 + (\sqrt{a}w)^2)$$

which tells us that we need to multiply the pressure by α while multiplying each of the velocity components with $\sqrt{\alpha}$.

What rests us is to define α in terms of $-\frac{1}{2}\pi \leq \theta \leq \frac{1}{2}\pi$ and $0 \leq r \leq \infty$. To determine the θ dependence the axial shock front speed is compared with the horizontal shock front speed as determined from the schlieren images. These speeds give us the ratio of the shock front pressures by the Rankine-Hugoniot conditions and therefore our weakening factor along the laser

axis.

$$\begin{aligned} v_{\text{cylindrical}} &= 4001\,\text{m}\,\text{s}^{-1} \\ v_{\text{spherical}} &= 1324\,\text{m}\,\text{s}^{-1} \\ &\Rightarrow\ \alpha(r_{\text{peak}}, \pm\frac{1}{2}\pi) = 0.10 \end{aligned}$$

Recall that we defined $r_{\text{peak}} = 1.5\,\text{mm}$ as the position of the shock front in the source state chosen from the best fit one dimensional simulation. As the horizontal shock front is already fitted to the experimentally determined shock front no weakening is necessary in that direction, so $\alpha(r_{\text{peak}}, 0) = 1$. We now need a smooth function of θ that interpolates between these two values of α. An obvious function fulfilling this requirement is

$$\alpha(r_{\text{peak}}, \theta) = (1 - \alpha(r_{\text{peak}}, \pm\frac{1}{2}\pi))\cos\theta + \alpha(r_{\text{peak}}, \pm\frac{1}{2}\pi)$$

The weakening at the shock front is now determined but has yet to be turned into a smooth function of r. Since it is preferable not to distort the stabilization of the hot plasma present at $r = 0$ we need $\alpha(0, \theta) = 1$. Knowing now the value of the weakening factor α at the edges $r = 0$ and $r = r_{\text{peak}}$ a sharp exponential function is used to interpolate between these in the space between the hot plasma and the shock front.

$$\alpha(r, \theta) = \alpha(r_{\text{peak}}, \theta) + (1 - \alpha(r_{\text{peak}}, \theta))e^{-\left(\frac{r}{1.3\,\text{mm}}\right)^{10}}$$

This leaves the plasma untouched while weakening across the entire length of the shock front. The weakening procedure is illustrated in figure 4.7.

After the appropriate weakening has been applied the 'best guess' initial condition is ready for a three dimensional simulation. The energy deposited by the laser that has not been used for ionization can be calculated from the constructed initial condition. The result is 58 mJ of energy, which at the time of interpolation is distributed as 16 mJ of kinetic energy and 42 mJ of thermal energy.

4.3 Verification of the Three Dimensional Simulation

The initial condition as described in the previous section is loaded into Comsol and a high mach number laminar flow simulation is performed.

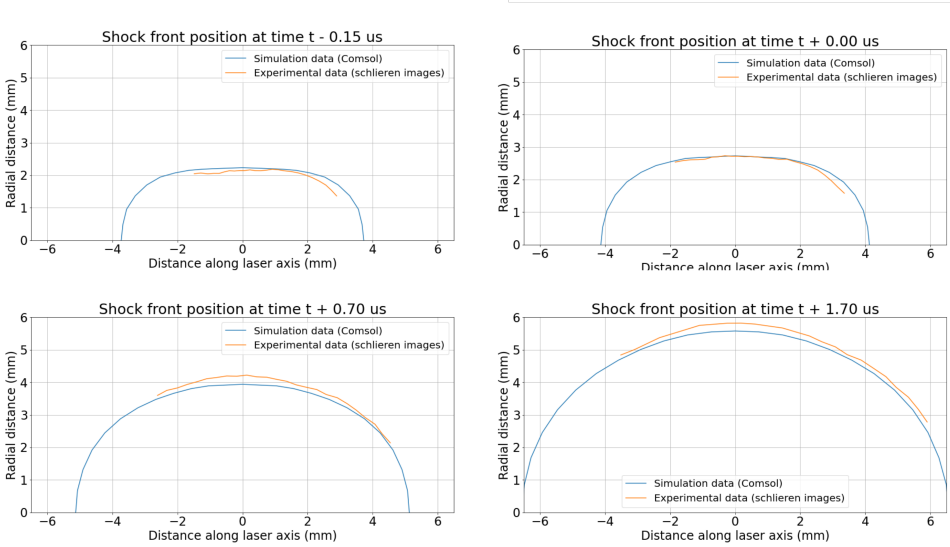

Figure 4.8: *Comparison between the shock front position as determined from the schlieren images and the position computed by simulation. $t = 0$ does not correspond with the laser pulse but with the time at which the radial position of the shock front is chosen to be sufficiently equal to allow comparison.*

Although Comsol has trouble converging when the pressure values at the start of the simulation are too high, we have circumvented this problem by choosing a time for the source state late enough ($t_{\text{source}} = 0.196\,\mu\text{s}$ and $r_{\text{peak}} = 1.50\,\text{mm}$) to make sure the pressure close to $r = 0$ has collapsed far enough. The resulting shock front of the two dimensional axi-symmetrical simulation is verified by making a comparison with the schlieren data (figure 4.8) while the torus formation is compared with the CCD intensity images (figure 4.10).

As can be seen the simulation with the reconstructed three dimensional initial condition indeed shows torus formation and splitting, confirming our hypothesis that the strong shock front is responsible for torus formation. However, making a good comparison between the simulated torus formation and the experimentally determined CCD intensity images is not straightforward.

First of all the CCD images do not capture the simulated two dimensional axi-symmetric images, instead, they capture a side view of the complete torus. If we assume the plasma is optically thin by the time torus formation starts this means the CCD intensity images are projections of the torus on a two dimensional plane. The problem of taking a two dimensional

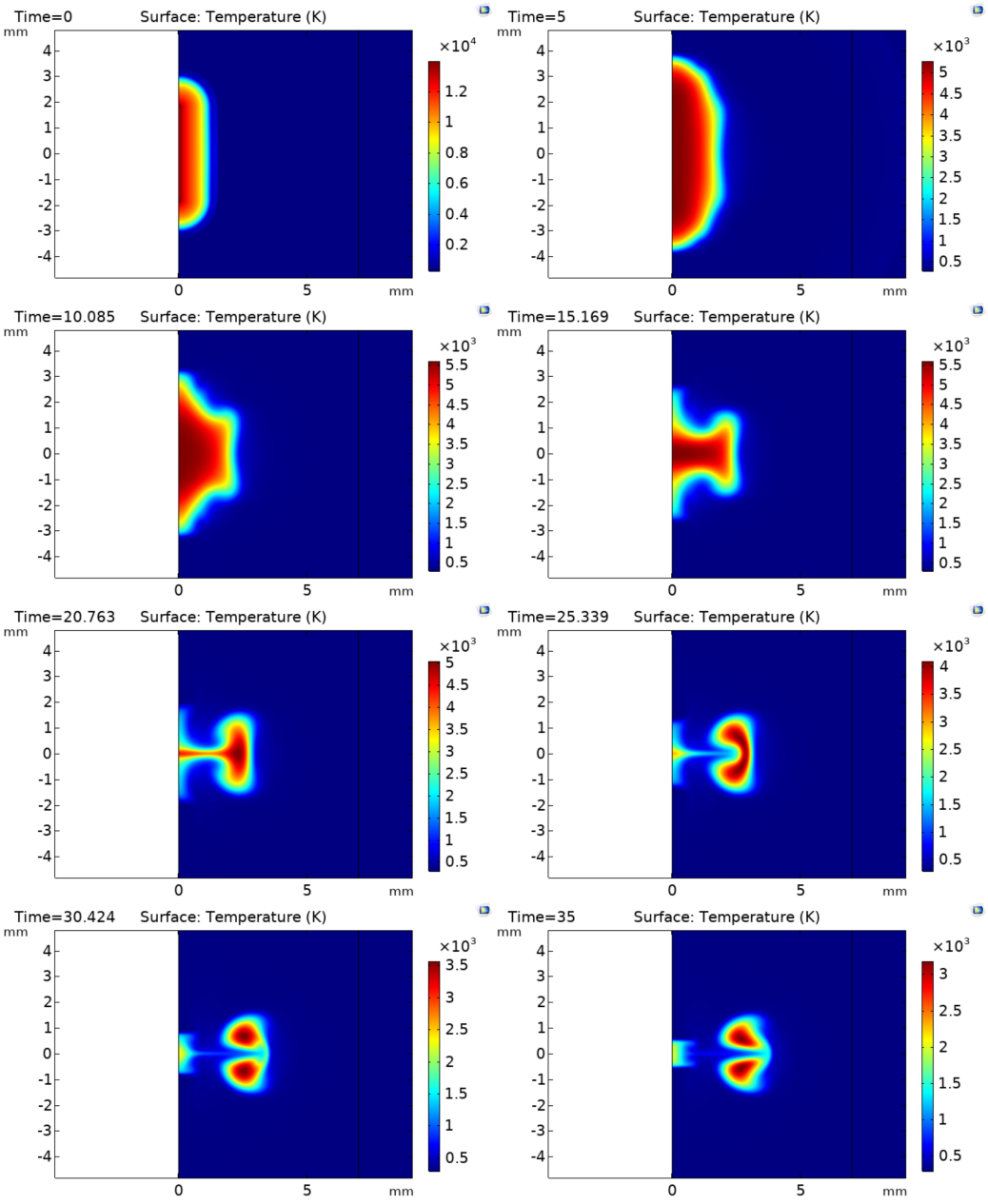

Figure 4.9: *Temperature (K) profiles produced by a Comsol axi-symmetric simulation. The starting condition is produced from the one dimensional simulation results as explained in the text. Both torus formation and splitting are observed. The time values shown are in microseconds. In figure 4.10 this data is used to make a comparison with the experimental CCD intensity data.*

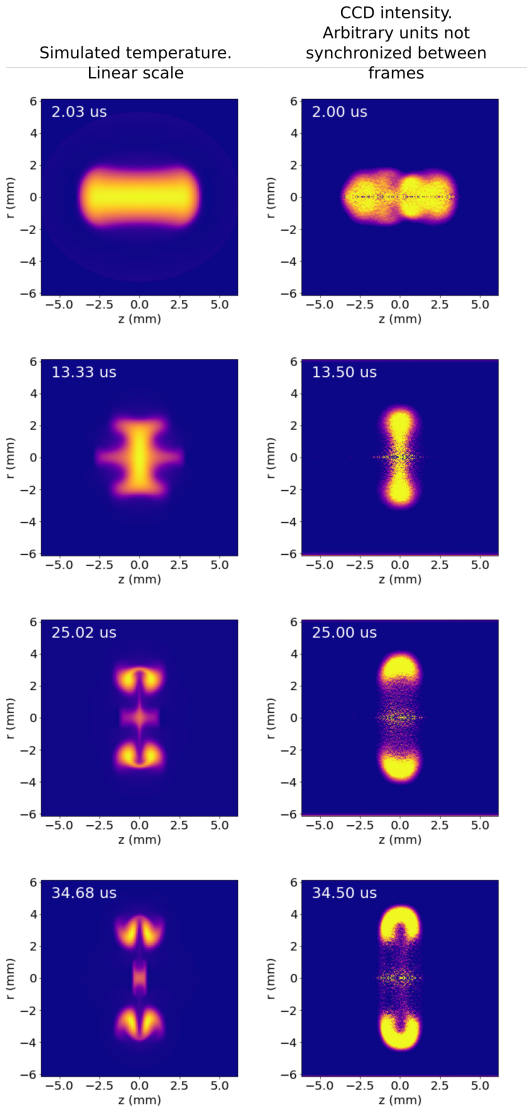

Figure 4.10: *Intensity between simulated temperature and experimental intensity images. The initial condition expands to the same size as seen on the intensity images. The splitting appears to happen sooner in the simulation. Also the simulated plasma appears less thick.*

projection and reconstructing a slice of a cylindrically symmetric three dimensional object is well studied. The method needed to achieve this is called an inverse abel transform, and high quality free software packages are available to perform this transform. In this project the software package PyAbel [8] is used to perform the inverse abel transform.

Another reason why the comparison is not trivial is the unknown radiation profile of the plasma. It is not clear how an intensity value in the CCD image corresponds to the temperature and density of the plasma. One way to deal with this problem is to assume the CCD intensity values are proportional to the amount of free electrons. If the plasma is a thermal plasma, which means the electron temperature and Helium gas temperature are in equilibrium, the electron density profile can be computed from the known temperature and pressure using the ideal gas law and the Saha equation.

4.4 Explanation for Observed Torus Formation and Splitting

Having successfully reproduced torus formation in a numerical study, the question now arises what is the process that causes the plasma to start its outward motion. Pressure profiles made at 7.5 µs show an area of low pressure following the strong shock front perpendicularly to the laser axis. Interestingly enough this low pressure area assumes pressure values under atmospheric pressure, meaning the gas is actually expanded compared to the ambient gas.

To gain more insight in the way the gas reacts to this moving low pressure area the pressure profile is augmented with either a velocity arrow field or the particle streamlines, see figure 4.11. The velocity field clearly indicates that, outside the shock front, the highest velocity values are found close to the origin, where at this time the plasma resides. By symmetry the gas flow flowing down the laser axis and the gas flow flowing up the laser axis are equally strong, and at the point where this gas flow meets the flow turns necessarily outward and pulls the plasma along.

The streamlines in figure 4.11 give an even greater insight in the gas flow. The helium particles making it through the shock front are either pulled around the low pressure area or pulled straight through it depending on their position. The particles going through the low pressure area move towards the laser axis, until they come close to the strong gas flow paral-

lel to the laser axis mentioned earlier. At this point the particle's velocity together with the strong axial flow give rise to an area of strong vorticity.

As can be seen in the third image in figure 4.11 the particles moving around the low pressure area do not end up in the high vorticity area. Instead, they follow the strong gas flow parallel to the laser axis and move between the high vorticity areas.

By these observations it is reasonable to conclude that the outward motion of the plasma is caused by the same process that causes its splitting, namely the collision of strong gas flow near the origin that causes a motion of the gas perpendicular to the laser axis. The strong flow appears as a result of the gas being pressed towards the below atmospheric pressure area 'dragged' behind the shock front.

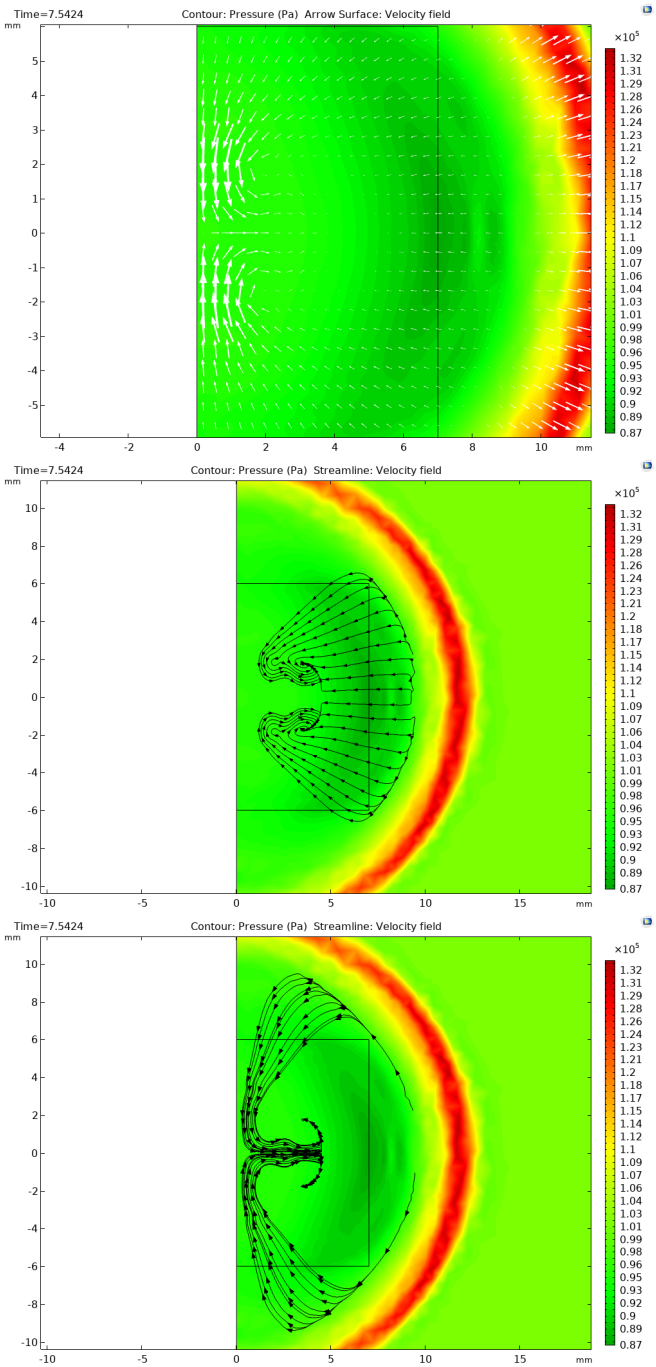

Figure 4.11: *The torus formation seems to be caused by a low pressure area that is dragged behind the strong shock front moving perpendicular to the laser axis. The velocity arrow field in the first image shows the gas to be moving fast close to the origin, pushing the plasma outwards. The second and third images show streamlines going through and around the low pressure area. The streamlines visible in the second image end up in an area of strong vorticity.*

Chapter 5

Improving the Heat Confinement of the Toroid

Without an external source of energy the plasma eventually loses its heat to its surroundings and extinguishes. To use the plasma in practical applications its lifetime must be extended. In this chapter the decay of the plasma intensity is studied and we argue that the plasma reaches local thermodynamic equilibrium (LTE) before 10 µs. LTE means that the electrons have transferred their energy to the Helium atoms such that both species are at the same temperature. It is argued that the dominant process cooling the plasma is the exchange of cold and hot particles at the surface of the plasma (ambipolar diffusion).

The rate at which the ambipolar diffusion is able to cool the plasma is related to the plasma geometry. It is shown using the intensity of the plasma as a function of time that this rate accelerates greatly after the plasma is split.

This thesis is made as part of a research project with the goal of heating the resulting plasma torus using a microwave cavity. This chapter supports this goal in two ways. First it is attempted to alter the surroundings of the plasma in such a way that the plasma maintains its torus shape while preventing the splitting. Also the LTE of the plasma is used to validate the use of the Saha equation to calculate the electron density. This electron density can be used in subsequent research to calculate resistivity values for the plasma and the effect of the microwave fields on the plasma temperature.

5.1 Arguments for local thermodynamic equilibrium

Argument based on the number of electron collisions

Consider an electron moving through the plasma. Assuming the helium atoms behave as hard spheres with a certain kinetic radius r we determine the average distance the electron will travel before a collision with a neutral. Since the electron speeds are much higher than the ion speeds we will assume the atoms are standing still.

Following [9] consider a 'slab' of gas with frontal area A and thickness dx containing n atoms per unit volume. If the Helium atoms have cross sectional area πr_{He}^2 the chance that the electron moving through the gas hits one of the atoms is

$$\frac{\text{area blocked by atoms}}{\text{total area}} = \frac{nAdx \cdot \pi r_{\text{He}}^2}{A} = n\pi r_{\text{He}}^2 dx$$

Therefore if we start out with N_0 particles, every distance dx we lose a fraction $-n\pi r_{\text{He}}^2$

$$\frac{\mathrm{d}N}{\mathrm{d}x} = -n\pi r_{\text{He}}^2 N$$

Which tells us $N = N_0 e^{-\pi n r_{\text{He}}^2 x}$. At a distance x we lose $\frac{\mathrm{d}N}{\mathrm{d}x}\mathrm{d}x$ particles, which means the average distance the particles travel is

$$\lambda = -\frac{1}{N_0}\int_0^\infty x\frac{\mathrm{d}N}{\mathrm{d}x}\mathrm{d}x = -\int_0^\infty x de^{-\pi n r_{\text{He}}^2 x} = \frac{1}{\pi n r_{\text{He}}^2}$$

Literature often quotes an extra factor of $\sqrt{2}$ in the denominator. This factor only appears when the moving particle is considered to be indistinguishable from the obstructing particles, and both are subject to a Maxwell-Boltzmann velocity distribution. So by our assumption of stationary helium atoms we lose this factor.

From the electron speed and the mean free path we can calculate the amount of collisions per unit time. To turn this number into an argument for the quick establishment of thermal equilibrium we also need to know how much energy an electron transfers in each collision. To compute this exactly we would need a deep dive into quantum mechanics, but to get the

Version of July 1, 2020– Created July 1, 2020 - 11:37

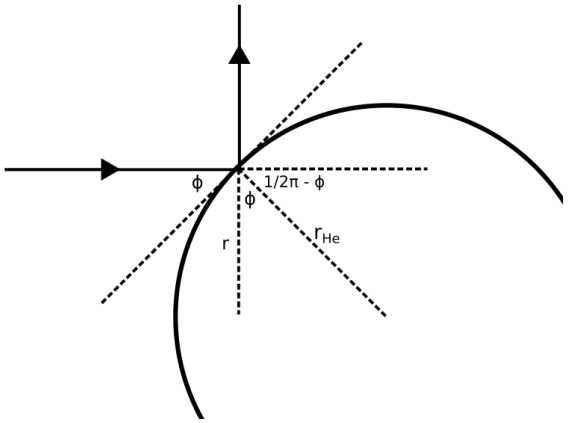

Figure 5.1: *The electrons are considered as fast moving point particles scattering of spherical Helium atoms with radius r_{He}.*

order of magnitude we use classical mechanics and consider the electrons as point particles scattering of a spherical helium atom.

From conservation of momentum one can see that the Helium atom after the collision will move along the line through the center of the sphere and the point of collision. We therefore calculate the electron speed along this line and apply the one dimensional result. The velocity of the electron in the direction of the radius of the sphere is

$$v' = v\cos\left(\frac{1}{2}\pi - \phi\right) = v\sin\phi$$

Substituting this speed into the one dimensional result of a two body collision gives us

$$v_{\mathrm{He}} = \frac{2m_e}{m_e + m_{\mathrm{He}}}v' = \frac{2m_e}{m_e + m_{\mathrm{He}}}\sin(\phi)v$$

So the energy transferred to the Helium atom is

$$E_{\mathrm{He}} = \frac{1}{2}m_{\mathrm{He}}v_{\mathrm{He}}^2 \approx \frac{2m_e^2}{m_{\mathrm{He}}}v^2 \cdot \sin(\phi)^2$$

To average the energy over the angle ϕ we note that every piece of frontal area of the Helium atom has the same chance to be hit. The chance that the electron hits at position r is therefore $\frac{2\pi r\mathrm{d}r}{\pi r_{\mathrm{He}}^2}$. From figure 5.1 one can see

$\cos\phi = \frac{r}{r_{\mathrm{He}}}$ so averaging over the different positions the electron can hit the Helium atom adds a factor of

$$\int_0^{r_{\mathrm{He}}} \frac{2\pi r dr}{\pi r_{\mathrm{He}}^2} \sin^2(\phi) = \int_0^{r_{\mathrm{He}}} \frac{2\pi r dr}{\pi r_{\mathrm{He}}^2} \left(1 - \left(\frac{r}{r_{\mathrm{He}}}\right)^2\right) = \frac{1}{2}$$

This tells us that the spherical scattering is half as effective at taking away electron energy compared with the one dimensional situation. The average energy transfer per collision is therefore

$$\langle E_{\mathrm{He}} \rangle = \frac{m_e^2}{m_{\mathrm{He}}} v^2 = \left(\frac{2m_e}{m_{\mathrm{He}}}\right) \cdot \frac{1}{2} m_e v^2 \tag{5.1}$$

Equations 5.1 and 5.1 together can give us insight into how quickly a fast moving electron will transfer its energy to the Helium gas. To compute λ we consult our three dimensional simulation results after the laser has finished expanding ($t \approx 5\,\mu\mathrm{s}$) and use the values $T \approx 6 \times 10^3\,\mathrm{K}$ and $p \approx 8.4 \times 10^3\,\mathrm{Pa}$ found in the plasma. For a lower bound on the speed of the electrons we compute the electron mean speed from this temperature as well (higher speeds will only accelerate cooldown).

$$n \approx 1 \times 10^{24}\,\mathrm{m}^{-1}$$
$$\lambda \approx 1.9 \times 10^{-5}\,\mathrm{m}$$
$$v_e \approx 4.8 \times 10^5\,\mathrm{m\,s}^{-1}$$

Finally from literature [10] we find a kinetic radius of 130pm for Helium.

$$\frac{\langle E_{\mathrm{He}} \rangle}{E_e} = \frac{2m_e}{m_{\mathrm{He}}} \approx 3 \times 10^{-4} \qquad \nu = \frac{v_e}{\lambda} \approx 3 \times 10^{10}\,\mathrm{s}^{-1}$$

Based on these numbers we expect the electrons to lose their energy in the order of $10^{-7} \sim 10^{-6}$ s. Note that we have only considered collisions with neutral helium atoms, while in fact some of the collisions will be between electrons and Helium ions. For our argument it does not matter how many collisions are with ions exactly, but it's important to note that the presence of ions will not allow the electrons to retain their temperature longer. To see this consider that the attractive electromagnetic force between the ions and the electrons causes the Helium ions to effectively have a larger radius than the neutral atoms, therefore making ν even bigger than it already is and accelerating the electron cooldown.

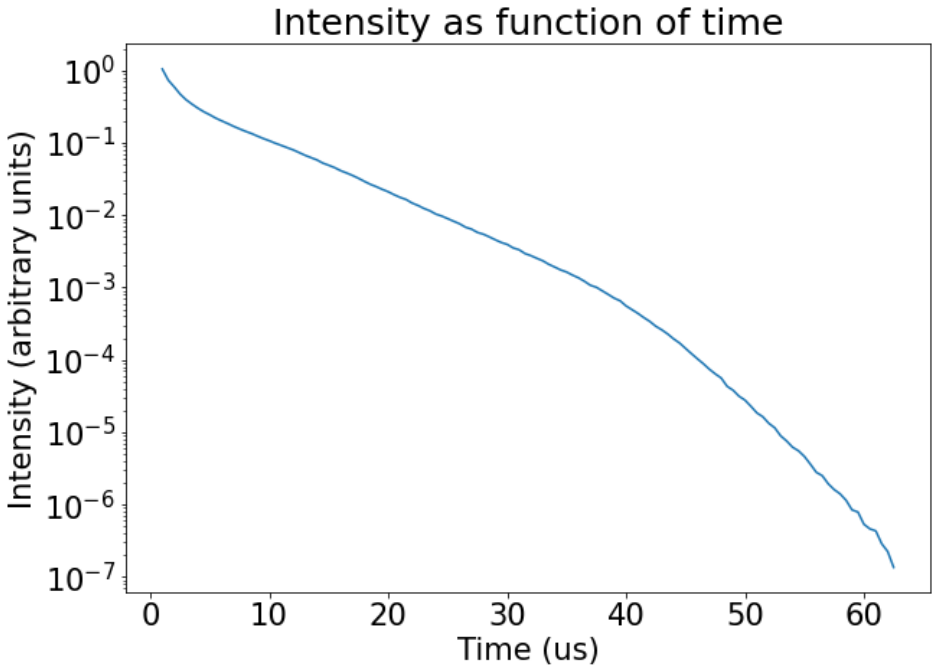

Figure 5.2: *The intensity of the plasma emission as a function of the time after the laser pulse. This data is produced by taking multiple CCD images and normalizing them with respect to the first. Data kindly provided by Vincent Kooij.*

Argument based on the measured plasma intensity

A second way to see the plasma is likely to be in local thermodynamic equilibrium is to consider the intensity of the plasma over time. Even though we do not know exactly how the plasma properties correspond to the CCD intensity values, we know that the electrons will move through the plasma at much higher speeds than the Helium ions do. The electromagnetic radiation seen by the CCD camera is therefore primarily produced by the electrons. This suggest that the electromagnetic radiation intensity will be proportional to the electron density. Therefore, the intensity of the plasma over time (figure 5.2) tells us how the electron density changes.

If the electrons are much hotter than the neutral helium atoms we expect their number densities to be higher than expected after the electron temperature has fallen. The reason for this is that there is more energy available for the ionization of electrons. However, as the electrons and ions lose energy their numbers will start to fall and eventually reach towards

the values expected by the Saha equation at LTE. The primary process responsible for decreasing the electron and ion number densities is recombination in which an electron and ion combine to form again a neutral atom. We therefore expect (following [9]) that the electron density will fall in time proportional to the amount of electrons and ions present

$$\frac{\partial n_e}{\partial t} \propto -n_e n_i \approx -n_e^2$$

Taking α as our constant of proportionality it is not hard to verify that the solution to this equation is

$$n_e = \frac{\alpha}{t}$$

.

As the plasma reaches LTE the electrons inside the plasma have, besides radiation losses, no way to lower their temperature. The primary way of the plasma to lose heat is diffusion, in which hot particles and cold particles are exchanged at the boundary of the plasma. The mathematics in this case is more involved (again see [9]) but the important result in our case is that the electron density is expected to fall around with time, where the decay constant is dependent on the plasma geometry.

With these results in hand we turn to our intensity graph, and see whether the graph indeed passes from $\frac{1}{t}$ decay to exponential decay suggesting that the plasma assumes LTE. In fact, this is exactly what is visible at the start of the intensity graph in figure 5.2. In figures 5.3 fits of the expected electron density functions are attempted at different times after the laser pulse, showing clearly that the $\frac{1}{t}$ fit is very good shortly after the laser pulse while the plasma assumes exponential decay at later times. From the figure it can also be seen that the $\frac{1}{t}$ fit starts to become less good as time approaches 10 µs suggesting LTE is established around this time.

A second property of our intensity function we expect based on our discussion of heat loss is a rapid decrease in intensity as the plasma undergoes splitting. At the time of splitting the plasma loses heat by diffusion so the rapid increase of surface area of the plasma should be detrimental to its heat containment. In figure 5.4 the decay constant of the intensity graph is shown as a function of time. This figure is produced by attempting an exponential fit at many points in time, and saving the exponential decay resulting from this fit. The vertical orange line shows the time at which the splitting of the plasma becomes visible in the CCD intensity images. The time of splitting clearly indicates the moment at which the decay constant

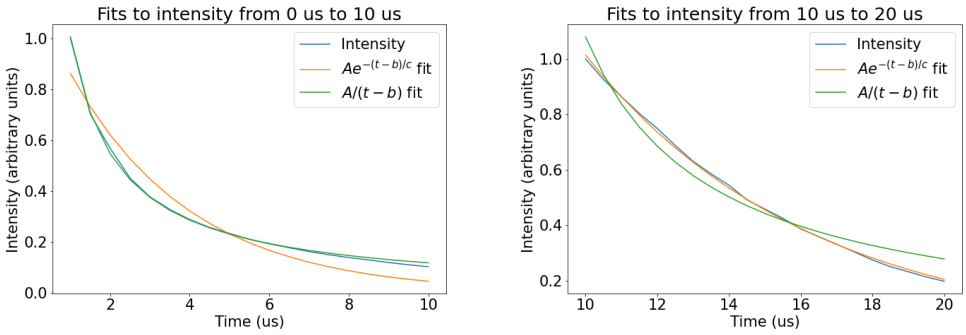

Figure 5.3: *Fits to parts of the intensity graph shown in figure 5.2. As motivated in the text the intensity of the plasma initially follows a $\frac{1}{t}$ decay suggesting an energy loss dominated by collisional recombination. At later times the decay becomes exponential as the plasma reaches local thermodynamic equilibrium and the cooling is dominated by ambipolar diffusion.*

goes over from a relatively constant value over time to a rapid decrease, in line with a diffusion dominated heat loss.

5.2 Electron density profile using the Saha equation

When equilibrium is established the degree of ionization and the temperature of the plasma are related by the Saha equation. We neglect doubly ionized helium atoms and focus on the singly ionized atoms, the motivation for this will become apparent later. The Saha equation reads

$$\frac{n_e^2}{n_0 - n_e} = \frac{2}{\lambda_e^3}\frac{g_1}{g_0}e^{-\frac{E_i}{kT}} \tag{5.2}$$

Here g_0 and g_1 are respectively the degeneracies of the ground state and the ionized state while n_e and n_0 are respectively the electron and neutral atoms particle densities. The wavelength appearing in the equation $\lambda_e = \sqrt{\frac{h^2}{2\pi m_e kT}}$ is the thermal de Broglie wavelength of an electron.

Assuming the ionized atom and the neutral atom are likely to be in their ground state, which will be the case for the temperatures observed, we can make the approximation $\frac{g_1}{g_0} \approx 2$. The reason for this is that the electron in the ionized helium ion has two position in the inner shell to be in. Furthermore we can neglect n_e relative to n_0 as long as the degree of ionization is

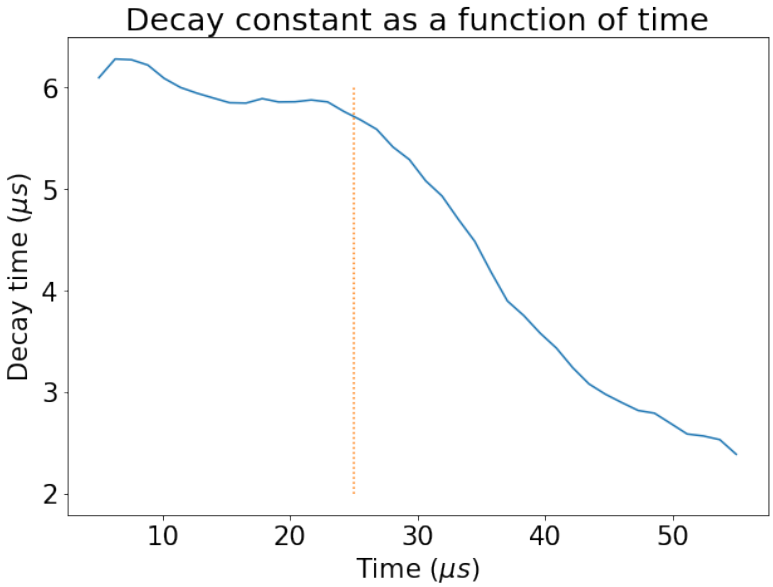

Figure 5.4: *At every point in time of figure 5.2 an exponential fit is attempted. The decay constants of the exponential fits are plotted as a function of time. The vertical orange line marks the time at which the splitting becomes visible in the CCD intensity images. Clearly it also marks the time at which the exponential decay accelerates greatly.*

low $\chi << 1$. Equation 5.2 can therefore be written as

$$n_e = \sqrt{\frac{4n_0}{\lambda^3} e^{-\frac{E_i}{kT}}}$$

Again using $\chi << 1$ a good approximation is to take n_0 equal to the particle density predicted by the ideal gas law.

$$n_e = \sqrt{\frac{4p}{\lambda^3 kT} e^{-\frac{E_i}{kT}}} \tag{5.3}$$

where p is the local pressure. It is now clear why we're allowed to neglect the doubly ionized Helium atoms. The second ionization energy for Helium is roughly twice as large as the first, therefore the number of doubly ionized atoms can be estimated by substituting $E_i \Rightarrow 2E_i$. But this is equivalent to multiplying n_e by $e^{-\frac{E_i}{kT}}$ which is much less than one for temperatures up to $10^5 K$.

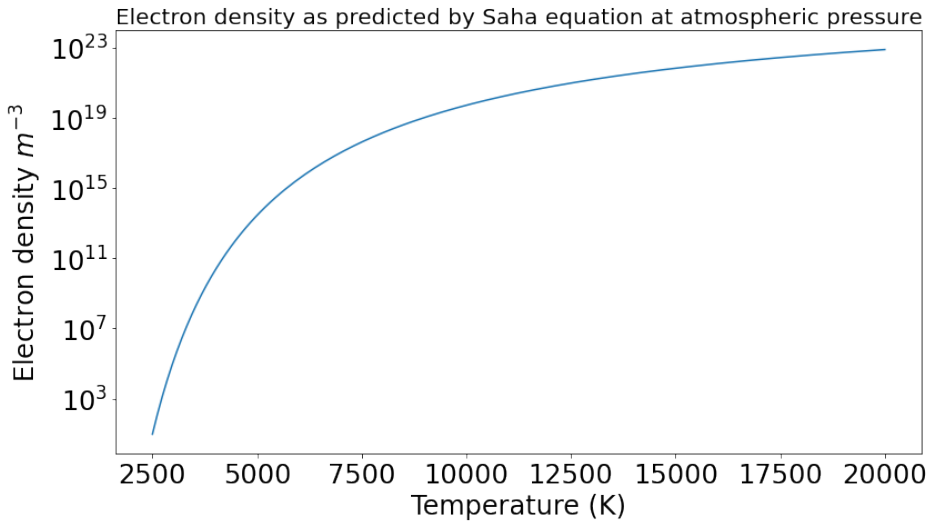

Figure 5.5: *Assuming local thermodynamic equilibrium and low degree of ionization the Saha equation can be combined with the ideal gas law to find the electron density as a function of temperature. At atmospheric pressure and the temperatures on the x-axis the neutral particle density will vary linearly from* $2.9 \times 10^{24}\,\mathrm{m}^{-3}$ *to* $3.7 \times 10^{23}\,\mathrm{m}^{-3}$ *meaning the the assumption of low degree of ionization starts to become invalid at the higher temperatures shown.*

5.3 Creating a toroidal vortex to prevent splitting

To prevent the splitting of the plasma, methods to passively influence the gas flow are examined.

At first this is attempted by placing a plate perpendicular to the laser axis close to the laser focus. A circular hole is made in this plate with the laser axis going through the center of the hole. The hole will pass only a small part of the outward moving shock front. This part of the shock front will spread out at the other side of the plate and thereby quickly diminish in power. As the shock front dies out the pressure at the side of the plate facing away from the plasma will revert to the ambient pressure and thereby forcing gas flow through the circular hole towards the lower pressure gas near the plasma. The axial gas inflow caused by the shock front which eventually splits the plasma will hopefully be impeded by the flow from the plate.

Simulations with different values for the distance of the plate to the plasma and the radius of the circular hole are attempted. The simulation that was most capable of retaining the plasma torus shape is presented in figure

5.6. This figure also shows the electron density of the plasma as computed with the Saha equation (equation 5.3).

Given that this method still features significant splitting of the plasma (see figure 5.6) an alternative method is studied as well. This method features a curved wall that acts as a shock front reflector. A part of the shock front is reflected and focussed close to the laser focus. This causes the upward moving gas flow to be stronger than the downward moving flow. Again, this causes a vortex that captures the plasma with an improved heat confinement compared with the previous simulation. Different values for the width, placement and focus point of the wall are considered and the best simulation is presented in figure 5.7.

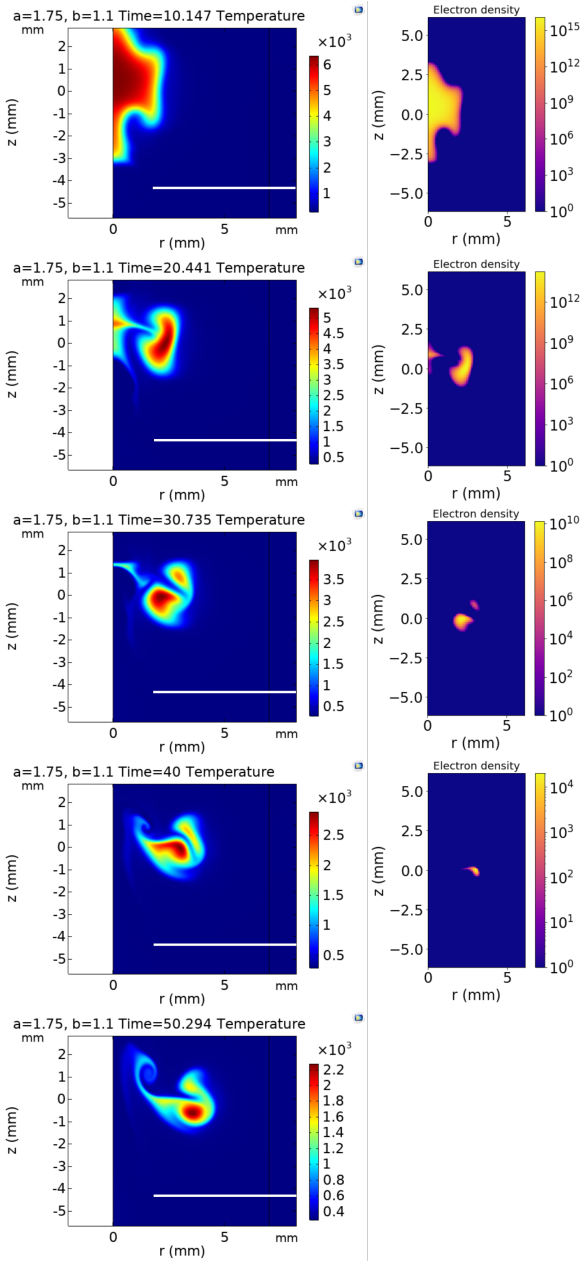

Figure 5.6: *A plate modeled as a thin immovable wall is placed close to the plasma (white horizontal line). The circular hole in the plate causes an upward moving gas flow which eventually captures the plasma in a vortex. The upward moving gas is visible especially well in the third image from the top. At the right hand side profiles of the electron density (unit* m^{-3}*) are made using equation 5.3. The wall is placed* 4.35 mm *from the laser focus and the aperture has a radius of* 1.75 mm.

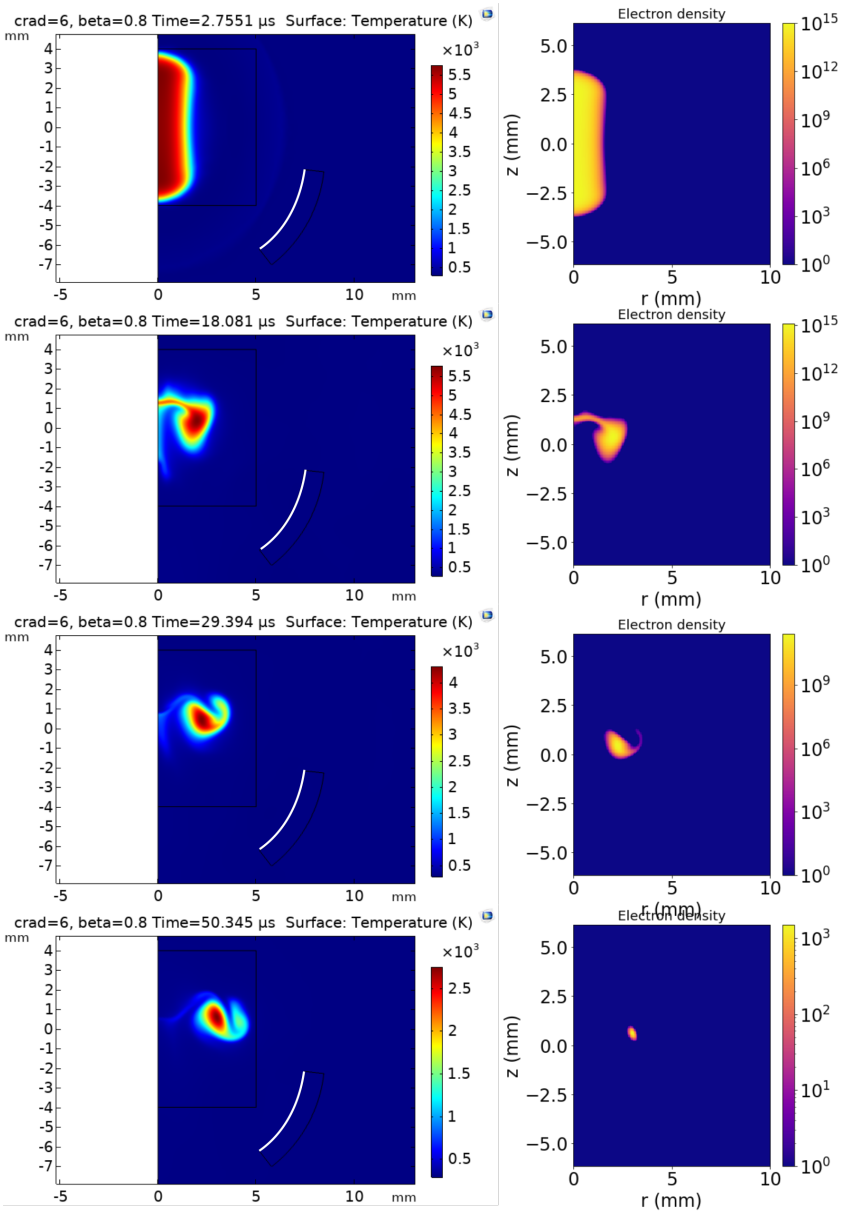

Figure 5.7: *A reflector is modelled as a curved wall of* 1 mm *thickness. The surface which reflects the shock front is marked by a white line. The reflected shock front causes a vortex that captures the plasma. This geometry features even less splitting than the simulation presented in figure 5.6. The electron density has units* m^{-3}*. The right images are electron densities computed using equation 5.3. The wall has a circular curvature focussed at* $r = 1.5\,\mathrm{mm}$*,* $z = -1.5\,\mathrm{mm}$*, with radius* 6 mm *and a width of* 0.8 rad*.*

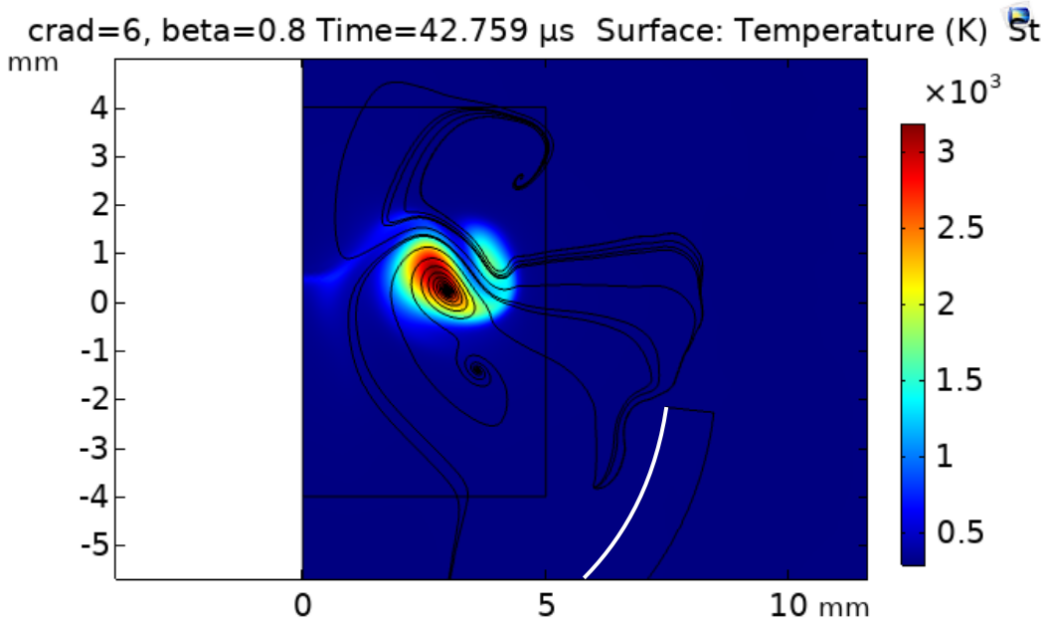

Figure 5.8: *Temperature profile of the plasma at* 43 µs *after the laser pulse. Streamlines following the gas flow velocity field are added to show the vortex in which the plasma is captured.*

Chapter 6

Discussion

This thesis is an investigation of the relatively recent observation that high power short focussed laser pulses result in an afterglow plasma with a toroidal shape. This process has the potential to see use in chemistry and is a first step towards a self-confined magnetohydrodynamics plasma. The process of torus formation has been reproduced by extensive computer simulations. The data used to verify the simulations come from an experimental setup using a 250 $\sim$ 275mJ, 10 ns laser pulse focussed at a Helium gas at atmospheric pressure. The simulations provided new insights in the physics of the laser induced flow.

The gas flow after the laser pulse has been shown to proceed in three major phases; the pressure collapse phase, the shock front formation phase and finally the shock front propagation phase. The strong shock fronts resulting from this process have been shown to eventually cause the torus formation. The primary cause of torus formation is a low pressure area behind the shock front moving radially outward along with the front. The plasma is pushed towards this low pressure area while being bounded at both sides by axial gas flow with strong vorticity.

The thermal and kinetic energy necessary to qualitatively reproduce the torus formation is found to be 58 mJ, meaning only a small part of the total laser energy is converted into thermal energy. The symmetric shape of the plasma suggests that a large part of the laser energy leaves the plasma without being absorbed. The remaining energy (max $\sim$ 200 mJ) is used for ionization and eventually exits the plasma in the form of radiation.

Two methods to prevent the cooling effect of the plasma splitting are pro-

posed and modeled. One method consists of placing a plate with a hole close to the plasma perpendicular to the laser axis. This plate has an effect on the gas flow that causes the plasma to be caught in a gas vortex.

Since a small part of the plasma is still split in this simulation, and since the gas dynamics close to the plasma have become more violent by the addition of the plate, the thermal energy of the plasma is not retained significantly better (see figures 4.9 and 5.6). However, it does improve the retention of the plasma torus shape that would otherwise be destroyed by the splitting process.

The second method is a spherical shock wave reflector which focusses a part of the shock front towards a point close to the laser focus. This method was more succesful in preventing the splitting of the plasma and therefore also retains the thermal energy for a longer period of time (see figures 5.6 and 5.7). The plasma torus shape is a favorable shape to induce circular currents which can heat the plasma and prevent it from extinguishing. Also, considering ambipolar diffusion the non-splitted plasma will have an improved heat confinement due to the higher diffusion gradient distances.

Finally, it is argued that without external heating the plasma reaches local thermodynamic equilibrium (LTE) before 10 µs. This time however is larger than the time predicted by collisional energy loss by hard sphere scattering $10^7 \sim 10^{-6}$. Possibly the crudeness of the hard sphere scattering approximation can explain this incompatibility. In any case a more detailed model of the energy transfer between the electrons and the Helium gas would be helpful. The knowledge of LTE justifies the use of the Saha equation which results in electron density profiles in the plasma. This data is valuable when heating of the plasma is attempted. However, the electron densities found in this way are different from the densities found in [11]. Therefore more research is needed to explain the source of the discrepancy.

While laser energy deposition had been studied numerically at least once [12] the simulation in this last study has an asymmetrical starting condition, which is not observed in our experimental setup. As the splitting of the torus is the result of the fairly symmetrical energy deposition of the laser in Helium, the splitting is a novel feature of the plasma not previously mentioned. This research contributes to the literature by explaining the torus formation, explaining the novel feature of plasma splitting and illustrating how the LTE of the plasma can be substantiated.

To reach the conclusions various numerical challenges were circumvented. The numerical challenges consist of numerical instability at $r = 0$, the very sharp shock fronts arising from the gas expansion and the large computation times necessary to simulate the torus formation in three dimensions. Remedies of these challenges might make it possible to perform simulations with an initial condition that more closely resembles the conical shape of the plasma shortly after the laser pulse. Potentially the first and third numerical challenges can be addressed by using an implicit time stepping scheme for the one dimensional simulation as opposed to the explicit time stepping scheme used in this thesis. Also, further research might try to shed light on the electron densities before LTE is established and find methods to heat the plasma in order to extend its lifetime.

Bibliography

[1] W. Bongers et al., *Plasma-driven dissociation of CO2 for fuel synthesis*, Plasma Processes and Polymers (2016).

[2] C. B. Smiet et al., *Self-Organizing Knotted Magnetic Structures in Plasma*, Physical Review Letters (2015).

[3] J. Blazek, *Computation Fluid Dynamics: Principles and Applications*, (2006).

[4] J. Kestin and W. Leidenfrost, *The Viscosity of Helium*, Physica (1959).

[5] F. Guevara, B. McInteer, and W. Wageman, *High Temperature Viscosity Ratios for Hydrogen, Helium, Argon, and Nitrogen*, Physics of Fluids **12** (1969).

[6] A. Achterberg et al., *Astrophysical Hydrodynamics and Gas Dynamics*.

[7] E. Jones, T. Oliphant, and P. Peterson, *SciPy: Open Source Scientific Tools for Python*, (2001 - present).

[8] S. Gibson, D. D. Hickstein, R. Yurchak, M. Ryazanov, D. Das, and G. Shih, *PyAbel*, 2019.

[9] F. F. Chen, *Introduction to Plasma Physics and Controlled Fusion*, (2016).

[10] N. Mehio, S. Dai, and D.-e. Jiang, *Quantum Mechanical Basis for Kinetic Diameters of Small Gaseous Molecules*, The Journal of Physical Chemistry (2014).

[11] D. van Seters, *RF Transmission Measurements on a Toroidal Laser-Induced Plasma*, (2019).

[12] S. Ghosh et al., *Numerical simulation of the fluid dynamic effects of laser energy deposition in air*, Journal of Fluid Mechanics **605** (2008).

[13] A. Achterberg, *Gas Dynamics*, Springer.

[14] J. F. Wendt, *Computational Fluid Dynamics: an Introduction*.

[15] M. Capitelli, A. Casavola, G. Colonna, and A. D. Giacomo, *Laser-induced plasma expansion: theoretical and experimental aspects*, (2003).

[16] T. Boudewijn, *Shock wave suppressed laser induced plasma*, (2017).

[17] M. Leins, *Development and Spectroscopic Investigation of a Microwave Plasma Source for the Decomposition of Waste Gases*, (2010).

[18] A. Bogaerts et al., *CO 2 conversion by plasma technology: insights from modeling the plasma chemistry and plasma reactor design*, Plasma Sources Science and Technology (2017).

[19] E. E. Toro et al., *Riemann Solvers and Numerical Methods for Fluid Dynamics: a Practical Introduction*, (1999).

[20] J. P. Boyd et al., *Chebyshev and Fourier Spectral Methods*.

[21] K. W. Morton et al., *Numerical Solution of Partial Differential Equations*, (2005).

[22] A. Fridman et al., *Plasma Physics and Engineering*, (2011).

[23] G. Batchelor et al., *An Introduction to Fluid Dynamics*, (2002).

[24] T. Pedley et al., *Introduction to Fluid Dynamics*, (1996).

[25] D. M. Pozar et al., *Microwave Engineering*, (2012).